JOINT EUROPEAN TORUS JET

JET–P(92)47

S. Putvinskii
and JET Team

On the Plasma Confinement in the m = 1, n = 1 Kink Distorted Central Core

On the Plasma Confinement in the m = 1 , n = 1 Kink Distorted Central Core

S. Putvinskii and JET Team*

JET-Joint Undertaking, Culham Science Centre, OX14 3DB, Abingdon, UK

** See Annex*

Preprint of Paper to be submitted for publication in
Nuclear Fusion (Letter)

On the Plasma Confinement in the m = 1, n = 1 Kink Distorted Tokamak Central Core

S. Putvinskii
JET Joint Undertaking, Abingdon, Oxon, OX14 3EA, UK.

Abstract

It is shown that kink distortion of the magnetic axis, and as a consequence a variation of the magnetic field along magnetic surfaces in the toroidal direction, leads to a new type of "superbanana" particle orbits and can change drastically the classical particle and heat transport in the central core. The phenomena discussed below have a time scale of $\simeq 10^{-3}$ s. and seem to be too slow to affect the sawtooth crash process (which is an order of magnitude faster) but can dominate in evolution of the plasma parameters between crashes, "snakes" formation [1, 2] and other phenomena in the central plasma inside q = 1 magnetic surface.

The experimental observations in tokamaks [1, 3] show that under certain conditions a kink equilibrium can exist in the central core (q < 1), not only during sawtooth crash but in between crashes during rather long time of $\tau_{eq} \approx 1$ s. It is clear illuminated by "snakes" phenomena [1, 2] and sometimes can be seen on the 2D poloidal pattern of soft X-rays which shows in these cases slow rotation of a displaced central hot core in the poloidal direction with period of about 10 ms. One can expect that the stellarator-type kink equilibrium is a natural state of the central plasma with q < 1 at the magnetic axis and therefore it is worthwhile to study the plasma confinement in the kink distorted central core. It should be mentioned that in the large tokamaks with an elongated plasma the sawtooth inverse radius (q = 1) can be a substantial part of the plasma minor radius (up to 60% at JET) and plasma transport in the central core can affect the global plasma confinement.

The main effect of the kink perturbation on the plasma confinement is a toroidal variation of the magnetic field along the distorted magnetic surfaces. The effect is similar to the traditional toroidal field ripple transport, which has

been investigated in detail [4]. The MHD induced ripple transport has been studied before [5], but for high energy alpha-particles. It was shown that the threshold amplitude of the MHD perturbations for the stochastic diffusion is rather high especially for low mode numbers. Here we shall concentrate on the "ripple well trapped" diffusion of the thermal plasma.

We shall start with the magnetic field model for the central kink core. There are many papers devoted to the nonlinear kink equilibrium for m = 1, n = 1 instability [6 - 10] aimed to find self consistent island width. We assume that the kink equilibrium with magnetic axis,

$$R_a = R_o + \xi \cos(\varphi), \qquad (1)$$
$$Z_a = \xi \sin(\varphi),$$

does exist and consider the amplitude of the displacement, ξ, to be an input parameter. In Eq. (1) R_o is the major radius of unperturbed axis, φ - toroidal angle. The formalism can be simplified taking into account that the new magnetic axis (1) is actually a plane circuit (of the same radius R_o), tilted and displaced from the original tokamak axis. Using the new toroidal coordinate system ρ, υ, φ where ρ is distance from the new magnetic axis and the procedure developed in [11], one can easily obtain the solution of the equilibrium equations in series of small parameters $\varepsilon = \rho/R_o$ and $\Delta = \xi/R_o$. The leading terms essential for analytical estimations presented below are:

$$B_\varphi = B_o\ (1 - \Delta\cos(\varphi) - \varepsilon\cos(\vartheta)) + \ldots,$$
$$B_\vartheta = B_o \frac{\varepsilon}{q}(1 - \Delta\cos(\varphi) - \varepsilon\cos(\vartheta)) + \ldots, \qquad (2)$$
$$B_\rho = B_o\ \frac{\varepsilon\Delta}{2}\ \sin(\varphi) + \ldots,$$
$$p = p_o - \frac{B_o^2\varepsilon^2\beta_p}{4\pi q^2}(1 - \Delta\cos(\varphi)) + \ldots.$$

Here $\varepsilon = \rho/R_o$, $\Delta = \xi/R_o$, $q(\rho)$ is the safety factor, p_o plasma pressure at the magnetic axis, $\beta_p \sim d^2p/d\rho^2$. Numerical calculations of particle orbit has been performed for magnetic field included higher order terms up to ε^3, Δ^3.

Because of the toroidal variation of the magnetic field, $|B| \simeq B_\varphi$, toroidally trapped (banana) particles undergo a superbanana motion. The trajectory of the banana centre can be found from conservation of the invariant

$$J_{\parallel} = \oint v_{\parallel}\, dl = 2R_o v_o \int_{\vartheta_{min}}^{\vartheta_{max}} q\chi d\vartheta = const, \qquad (3)$$

where $\chi = v_{||}/v_o$, ϑ_{min}, ϑ_{max} - coordinates of the turning points ($\chi = 0$) and integration over ϑ in (3) is performed along the field line $\varphi = \varphi_b + q\vartheta$, where φ_b is the toroidal coordinate of the banana centre, $\vartheta = 0$. Small variation of the minor radius of the magnetic surfaces, $\rho \sim (1 - \Delta\cos(\varphi))^{1/2}$, can be neglected in (3). Using particle energy and magnetic moment conservations and Eq. 2, χ can be expressed in terms of ϑ and φ_b:

$$\chi^2 = \chi_o^2 - (1-\chi_o^2)\ \Delta\ (1-\cos(\varphi_b + q\vartheta)) - (1-\chi_o^2)(\varepsilon_o - \varepsilon\cos\vartheta). \qquad (4)$$

The subscript "0" in (4) corresponds to the initial values of variables ($\varphi = 0$, $\vartheta = 0$). Integration in (3) can be fulfilled analytically only for deeply trapped particles $\chi_o^2 << \varepsilon$ for which (3) gives the following relationship between radial and toroidal coordinate of the banana center:

$$\varepsilon = \varepsilon_o + \Delta(1-\cos(\varphi_b)). \qquad (5)$$

Using Eq. 2 we find that for deeply trapped particles that are bouncing near the minimum of the magnetic field $\vec{B}\ \nabla\ |B| = 0$,

$$\vartheta_b = -\frac{q\Delta}{\varepsilon}\ \sin(\varphi_b). \qquad (6)$$

Projection of the trajectories (5), (6) on the poloidal plane are slightly elongated ($q < 1$) ellipses.

Fig. 1 shows poloidal projections of particle orbits obtained by direct numerical integration of guiding center equations. The new "pineapple" orbits consist of particle bouncing over banana orbit and drift of the banana center. It was found that Eq. 5, 6 are good approximation for banana center orbit not only for deeply trapped particles but for all toroidally trapped particles $\chi^2 < 2\varepsilon$. On the contrary, all transit particles orbits are very close to the magnetic surfaces. It can be seen easily from (Eq. 3 for $\chi = \pm 1$).

The remarkable feature of the new orbits is that the width of the banana center orbit $\delta\varepsilon = 2\Delta$, does not depend on particle energy, charge or mass, and

therefore ions and electrons have the same deviation from the starting magnetic surface. The period of particle motion over the superbanana can be estimated as follows:

$$\tau_{orbit} \simeq 2\pi / \dot{\varphi}_b \simeq \frac{2\pi R_o (\varepsilon_o + \Delta)}{qV_{dr}} \qquad (7)$$

Here V_{dr} is the toroidal drift velocity. For typical JET plasma parameters R_o = 3m, B = 3T and particle energy E_i = 5-10 keV the period $\tau_{orbit} \simeq$ 1 - 2 ms.

The banana centre orbit width is sensitive to electric field. In the presence of electric field with electric potential $\phi = \phi_o\ (1 - \rho^2 / \rho_1^2)$, where ρ_1 is the radius of the q = 1 surface, Eq. 5 takes the form

$$\varepsilon - \varepsilon_o + \frac{2e\phi_o(\varepsilon^2 - \varepsilon_o^2)}{m\upsilon_o^2 \varepsilon_1^2} = \Delta\ (1 - \cos(\varphi_b)). \qquad (8)$$

The orbit width as function of electric field for particles started from the magnetic axis (ε_o = 0) is shown in Fig. 2. The maximum amplitude $\varepsilon = 8\Delta$ corresponds to the negative charge of the plasma center, $2e\phi_{cr} / m\upsilon_o^2 = -\rho_1^2 / 2R_o\xi$, above which, $\phi_o < \phi_{cr}$, the banana center orbit becomes toroidally trapped.

At a large axis displacement

$$\xi > \xi_{cr} = \begin{cases} \rho_1 / 3; & \phi_o = 0 \\ \rho_1 / 9; & \phi_o = \phi_{cr} \end{cases} \qquad (9)$$

the orbit width is larger than the minor radius of the central core and the banana particles are not confined at all.

At small amplitude of displacement, $\xi < \xi_{cr}$, pineapple orbits lead to enhanced transport in the central region. We shall estimate the diffusion rate at two limiting cases assuming $|\phi_o| << |\phi_{cr}|$. At the large effective scattering time $\tau_{eff} = \tau_{sc}\ (\varepsilon + \Delta) > \tau_{orbit}$, where τ_{sc} is 90° - Coulomb scattering time, the diffusion rate can be estimated as follows:

$$D = \frac{4\Delta^2 R_o^2}{\tau_{sc}(\varepsilon + \Delta)^{1/2}} \qquad (10)$$

At the low particle energy, $\tau_{orbit} >> \tau_{eff}$, particle free path is defined by effective scattering time

$$\lambda \approx \dot{\rho}\tau_{eff} \approx R_0 \Delta \dot{\varphi}_b \tau_{eff} \approx \Delta q V_{dr} \tau_{sc}$$

and diffusion rate is equal to

$$D = \frac{\Delta^2 q^2 V_{dr}^2 \tau_{sc}}{(\varepsilon+\Delta)^{1/2}} \qquad (11)$$

The diffusion rate as function of plasma temperature is shown in Fig. 3. The maximum diffusion rates occurs at $\tau_{orbit} \approx \tau_{sc}\,(\varepsilon + \Delta)$ or $qE\tau_{sc} = 2\pi R_0^2 \omega_c m$, when E is particle energy.

For ions $\tau_{sc} = \tau_{ii}$ and critical particle energy which corresponds to the transition from (10) to (11) is equal to

$$E_{cr} = (1.75 n_{19}\ R_0^2 B)^{2/5}$$

Here [E] = κeV, $n_{19} = n/10^{19}$, [B] = T. For JET plasma parameters R = 3m, B = 3T, n_{19} = 3, the last estimation gives $E_{cr} \simeq 10$ keV and $D_i\,(E_{cr}) \simeq 10^4\,\Delta^2$. At a reasonable displacement of $\Delta \simeq 0.03$, $D_i\,(E_{cr}) \simeq 10\ m^2/s$.

The critical energy for the electron is very high (40 keV for JET parameters) and at the typical plasma temperature the electron diffusivity is described by Eq. 10 with $\tau_{sc} = \tau_{ei}$. Because the electron diffusion rate is significantly less than the ion diffusion rate, the kinked plasma core will be charged negatively $|\phi_0| \simeq$ T/e with respect to the outer plasma. The resulting ambipolar diffusion rate is small

$$D_a = \frac{2D_i D_e}{D_i + D_e} \simeq 2D_e << D_i, \qquad (12)$$

but the ion heat conduction, $\chi_i \simeq D_i$, remains large. Using Eq. 10, 11, one can estimate ion energy confinement time in the JET central region, as $\tau_{Ei} \simeq \rho_i^2 / D_i \simeq 10$ ms, which is much smaller than the sawtooth period $\tau_{sT} \simeq 100$ ms. Therefore if there is a residual kink distortion of the magnetic axis, the ion temperature profile is expected to be flat inside q = 1 surface.

The estimations of the plasma transport coefficients, Eq. 10-12, are valid only for a small axis displacement $\xi/\rho_1 << \rho_1/R_o$, when $|\phi_o| << |\phi_{cr}|$. At the large displacement picture is much more compicated and needs a special analysis.

Finally, we can summarize that even small kink perturbations of the central core can change drastically particle orbits and the plasma transport inside the inversion radius. Although we have only considered the effect of m = 1, n = 1 mode on the plasma confinement in the central core region, the results are qualitatively valid for islands m, $n \neq 1$ as well.

ACKNOWLEDGEMENTS

The author would like to thank Drs. J.A. Wesson and H.J. de Blank for helpful discussions.

REFERENCES

[1] A. Weller, A.D. Cheetham, A.W. Edwards, R.D. Gill, et al., Phys. Rev. Lett. 59 (1987) 2303.

[2] R.D. Gill, A.W. Edwards, D. Pasini, A. Weller, Preprint, JET-P(91)(54)1991.

[3] G.L. Jahns, S. Ejima, R.J. Groabner, N.H. Brooks, et al., Nucl. Fus., 22(1982)1059

[4] P.N. Yushmanov, Review of Plasma Physics, edited by B.B. Kadomtsev, V. 16, 1987.

[5] R.B. White, H.E. Mynik, Phys. Fluids B, 1(1989)980.

[6] M.N. Rosenbluth, R.Y. Dagazian, P.H. Rutherford, Phys. Fl., 16 (1973)1894.

[7] R.D. Hazeltine, J.D. Meiss, P.J. Morrison, Phys. Fl., 29 (1986)1633.

[8] Avinash, R.J. Hastie, J.B. Taylor, S.C. Cowley, Phys. Rev. Lett. 59 (1987)2647.

[9] L.E. Zakharov, A.P. Smoliakov, A.A. Subbotin, Sov. Plasma Phys., 16 (1990)779.

[10] A. Thyagaraja, F.A. Haas, Phys. Fluids B, 3 (1990)580.

[11] V.D. Shafranov, Nucl. Fus. 4 (1964)232.

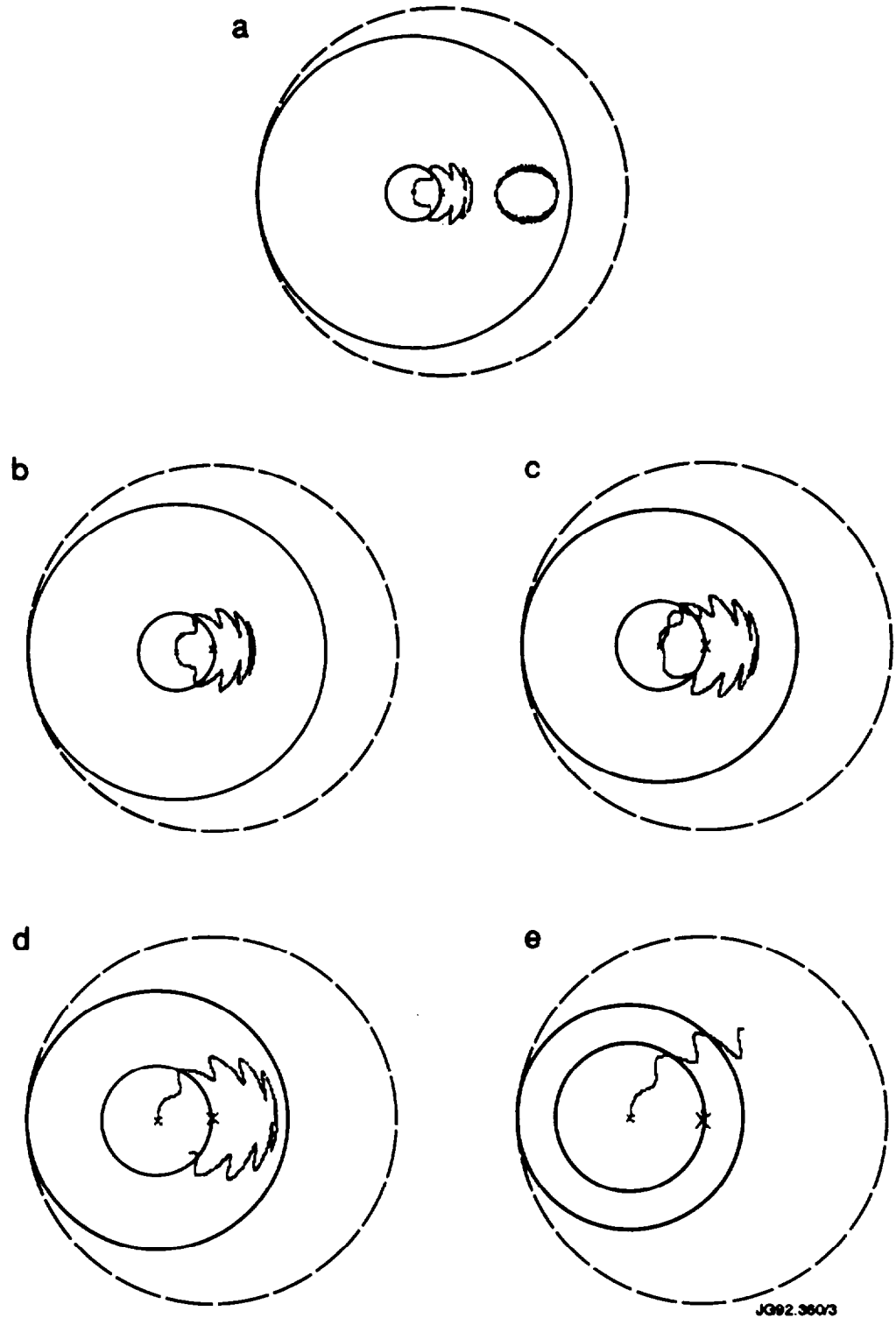

Fig. 1 Poloidal porojection of particle orbits starting from magnetic axis, $V_{||} = 0$, $\rho_L/\rho_1 = 0.05$, $\rho_1/R_0 = 0.15$.

a - $\Delta = 0.03$; b - $\Delta = 0.04$; c - $\Delta = 0.05$;
d - $\Delta = 0.06$; e - $\Delta = 0.08$;

Sign "X" marks the position of undistorted magnetic axis $R = R_0$.

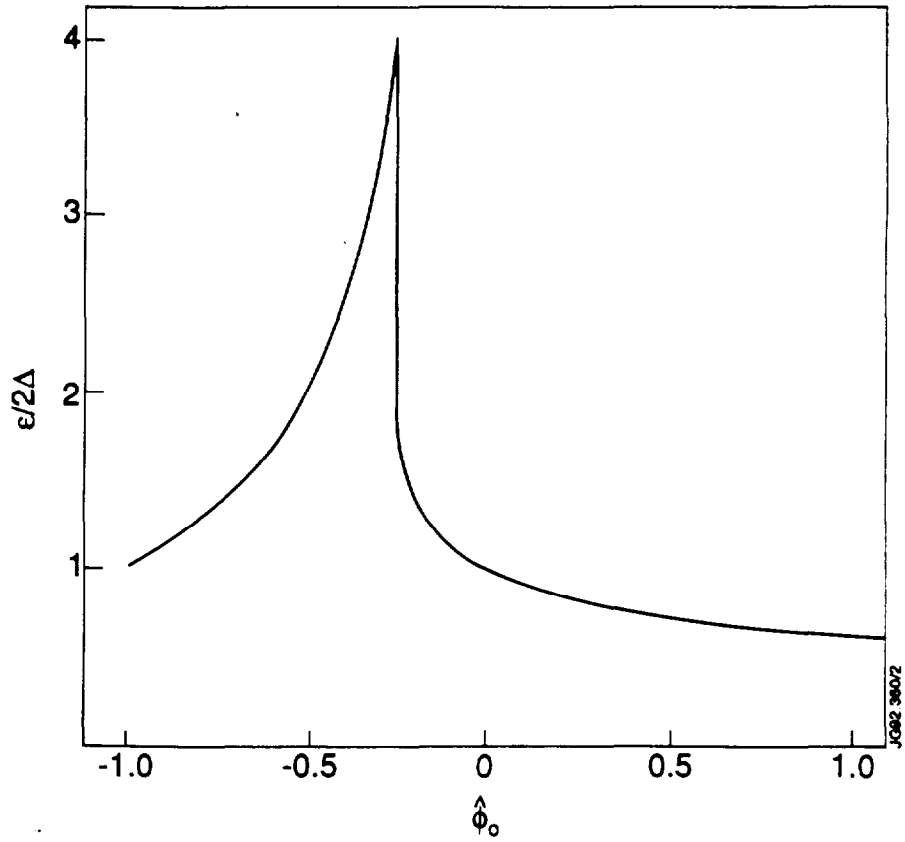

Fig. 2 Orbit width vs electric field, $\hat{\phi}_o = 4e\phi_o\Delta / mv^2\varepsilon_1^2$, for deply trapped particles, $V_{||} << (\varepsilon + \Delta)^{1/2}V$

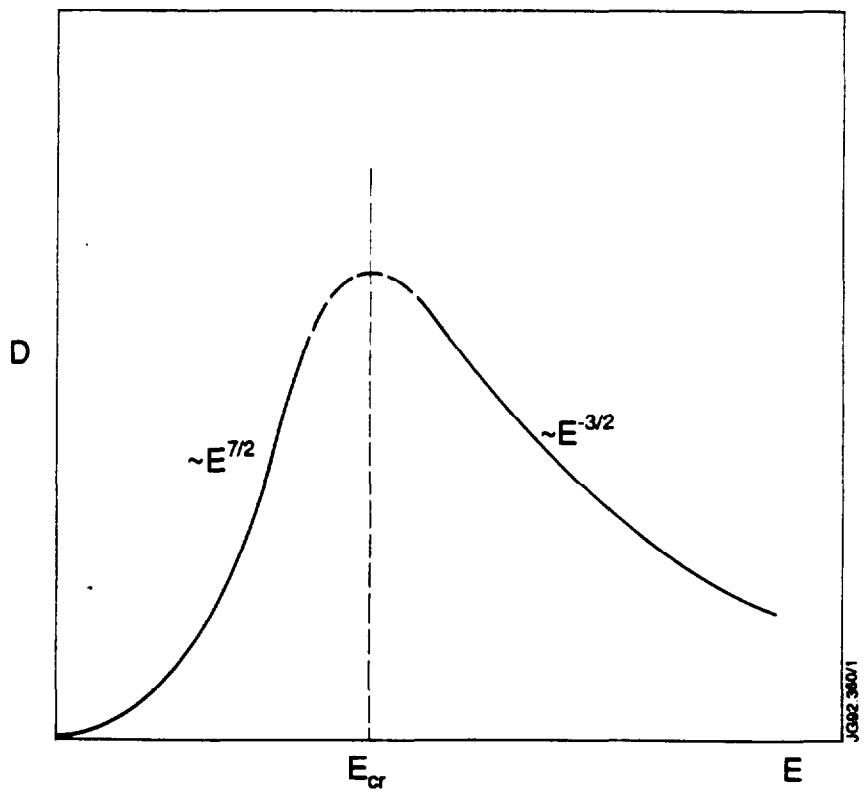

Fig. 3 Diffusion rate vs particle energy.

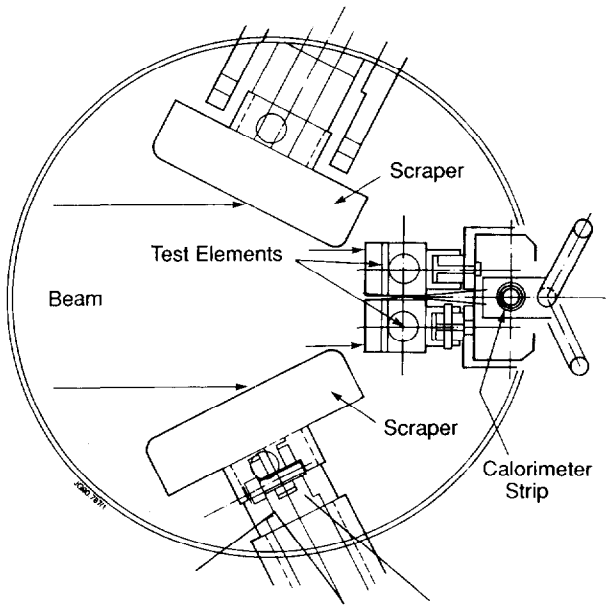

Fig. 7: Test set-up in the Beryllium test rig: The outer vertical edges of the elements are shielded by scrapers. The sections are rigidly mounted against a strong back. A calorimeter is installed behing the gap between the two elements.

section having the same external dimensions and using parallel connection for the coolant flow. The swirl tube section had two drillings of 10mm each with a twisted tape of twist ratio 2. Thermocouples where installed in the side wall, 3mm from the exposed surface. Fig 6 shows a schematic of both test sections.

4.4.2. Be Test Rig

The test sections are rigidly fixed against a strong back. The exposed area is 200 x 48mm². The outer edges of both vapotrons are behind the scrapers (Fig. 7).

5. Experimental results

5.1. Vapotron Heat Transfer

Power scans have been done with a vapotron and a swirl tube section installed side by side. The surface temperature of the test sections are shown in Fig.'s 8 and 9 as a function of the power density for two flow rates. The main effect of the higher flow rate is, in both cases, the extension of the operating range to higher power densities without excessive rise of the surface temperature. At power densities below 20MW/m², the surface temperature is the same for both flow rates. If anything, both panels are marginally colder at a given power density with the lower flow rate, indicating, that the gain in heat transfer with velocity is compensated by the higher viscosity due to the lower water

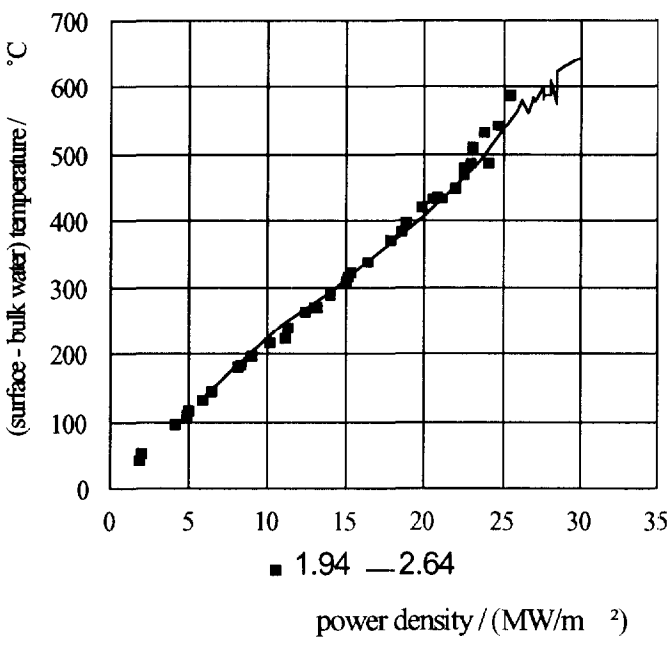

Fig.. 8: Vapotron surface temperature for water flow rates of 1.94 & 2.64 m³/h (8.5 & 11.6 m/s velocity)

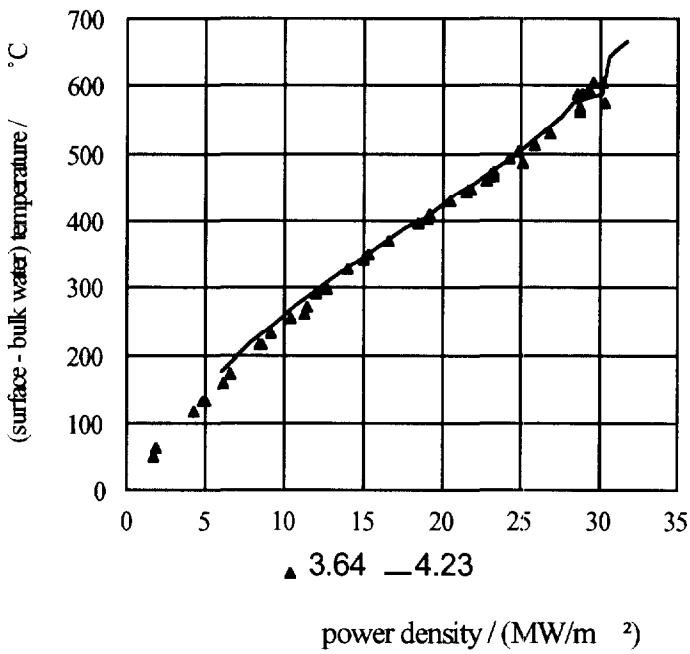

Fig. 9: Swirl tube surface temperature for water flow rates of 3.64 & 4.23 m³/h (7.4 & 8.6 m/s velocity)

temperature. In the case of the vapotron, the flow rates of 1.94 and 2.64m³/h correspond to a bulk water velocity of 8.4 and 11.5 m/s. The range of interest for the JET divertor is for a surface temperature up to 350 °C. This corresponds to a power density of approximately 17MW/m². At the low flow rate the highest absorbed energy was 0.509 MW with a pulse length of 4.86s.

5.2. Comparison Vapotron - swirl tube

The surface temperatures of the vapotron and the swirl tube section are almost identical (Fig. 10). The swirl tube has a slightly higher surface temperature up to 20MW/m². Above this power density the situation is reversed. The total power absorbed by both sections was almost identical. The higher temperature of the swirl tube section could again be explained (at least partially) by the higher flow rate and therefore lower water temperature. In the case of the swirl tube section we actually achieved the critical heat flux of 30MW/m² at the lower flow rate.

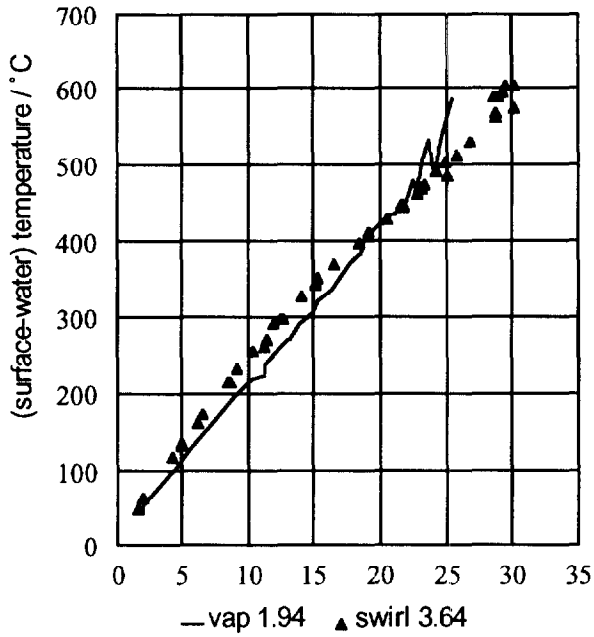

Fig. 10: Comparison vapotron (line) & swirl tube (symbols) for flow rates of 1.94 (vapotron) and 3.64 m³/h (swirl tube)

Table 3: Comparison of vapotron and swirl tube data: Δp: pressure drop at the quoted flow rate, ΔT_w: water temp. rise in °C, pump factor: flow x pressure (in Watt).

#40958	flow m³/h	$\frac{\Delta p}{bar}$	$\frac{power}{MW/m^2}$	ΔT_w	pump factor in Watt
vapotron	1.94	2.2	25.5	46.3	119
swirl tube	3.64	3.9	26.9	26	395

5.2.1. Pressure

Under operating conditions, vapotron and swirl tube compare as shown in table 3: The swirl tube needs nearly twice the flow and requires more than three times the pumping power. The vapotron produces twice the noise level at the water outlet compared to the swirl tube (Fig. 11) (actually, the noise levels at the in- and outlet of the swirl tube are roughly of the same magnitude and might both be created by the vapotron).

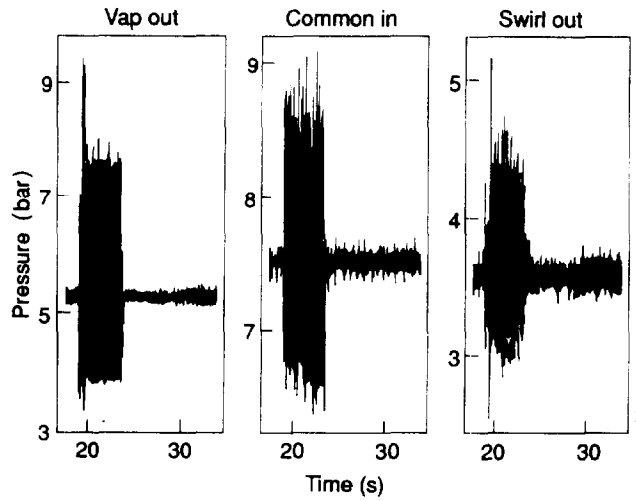

Fig. 11: Noise on the water pressure signals in bar for a high power pulse (data in table 3). Left: vapotron outlet pressure, middle: common inlet pressure, right: swirl tube outlet pressure

5.2.2. Surface temperature

Fig. 12 shows vertical profiles of the vapotron surface temperature for two pulses with 25.5 and 25.8MW/m². The water is flowing from top to bottom. The centre is clearly overheating in both cases and the profile is unsymmetrical, shifted in the direction of the water flow.

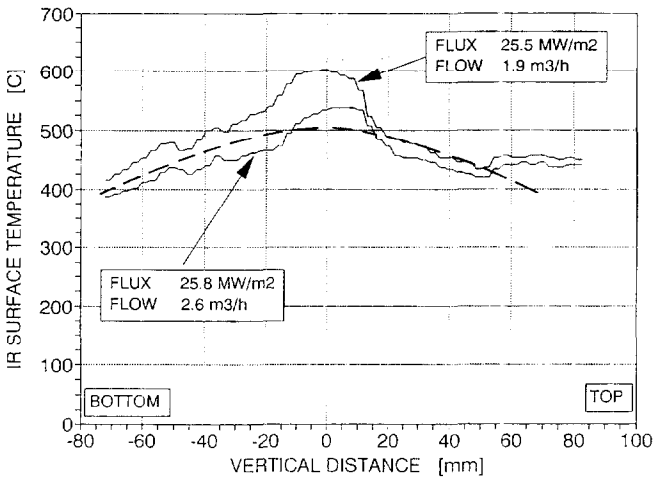

Fig. 12: Vertical profile of the vapotron surface temperature from the IR camera for a power density of 26MW/m². The dashed line is an eye fit to estimate the overheating

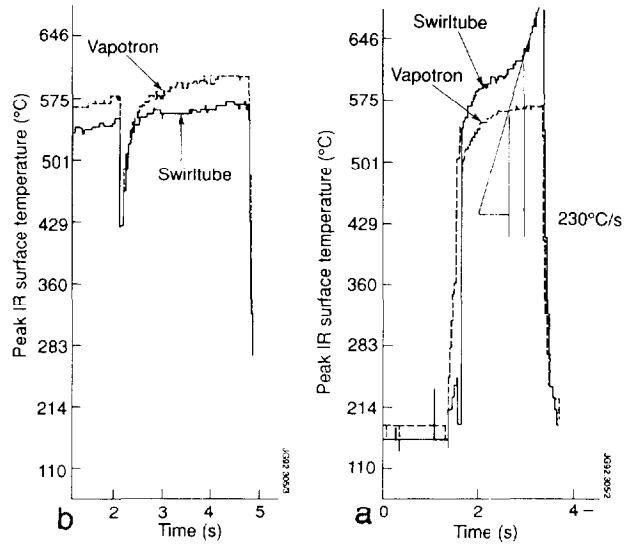

Fig. 13: Peak surface temperature from the IR camera, a) for the swirl section at critical heat flux (29.5MW/m²), and b) for the highest heat flux on the vapotron at 1.94m³/h for the pulse in table 3

This indicates insufficient subcooling. Increasing the flow rate from 1.9 to 2.6 m³/h reduces mainly the overheating in the centre and at the downstream end. This explains, why the vapotron shows higher surface temperatures with the low flow rate at high power densities in Fig. 8. The overheating is of the order of 100°C, as indicated by the dashed line in Fig. 12. In the case of the swirl tube we had two cases, where the temperature was running away. Fig. 13a shows the temperature rise measured with the IR camera at the hottest section of each element. The power density was 29.5 MW/m², the flow rate 3.58m³/h for the swirl tube and 27.5MW/m² and 2.64m³/h for the vapotron. The temperature rise at the surface of the swirl section is of the order of 230°C/s. Fig. 13b shows the vapotron surface temperature for the highest power density with the lower flow rate (25.5MW/m² and 1.94m³/h) together with the surface temperature of the swirl tube (26.9MW/m² and 3.68m³/h). The vapotron is clearly hotter, but still stable.

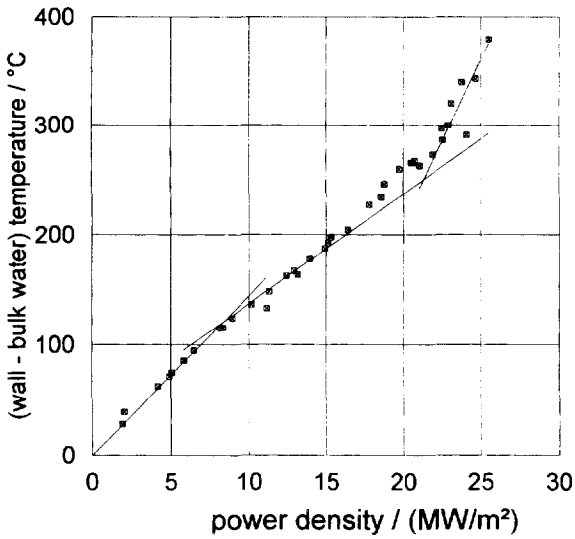

Fig. 14: Temperature difference in the vapotron across the heat exchange surface (wall - bulk water) for a flow of 1.94 m³/h

5.3. Vapotron at critical heat flux

As mentioned in 5.1, we did not take the vapotron to burnout, as the surface temperature at the high power level is well above that which is acceptable to us for other reasons. At power densities above 17MW/m² we can clearly see an excessive temperature rise in Fig. 14 of up to 100°C at the highest power density. This excessive temperature only occurs in the area with the peak power density (Fig. 12). The amount of overheating derived from Fig. 12 and 14 is identical. It is assumed, that the overheating is due to a locally over-critical heat flux which is stabilised by heat conduction into the fins. We have tested vapotrons to the

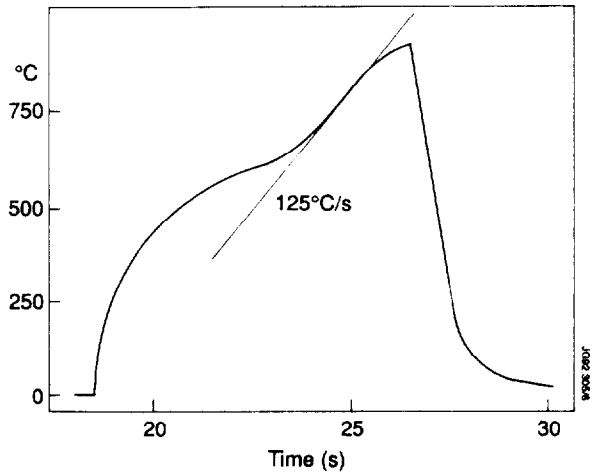

Fig. 15: TC temperature trace for a vapotron above the critical heat flux

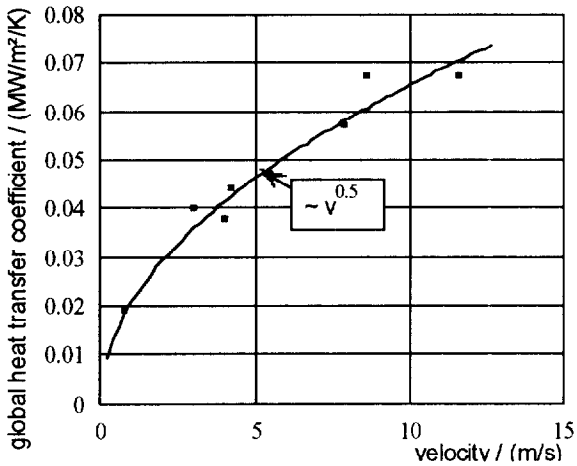

Fig. 17: Velocity dependence of the heat transfer in vapotrons with 4 mm fin height

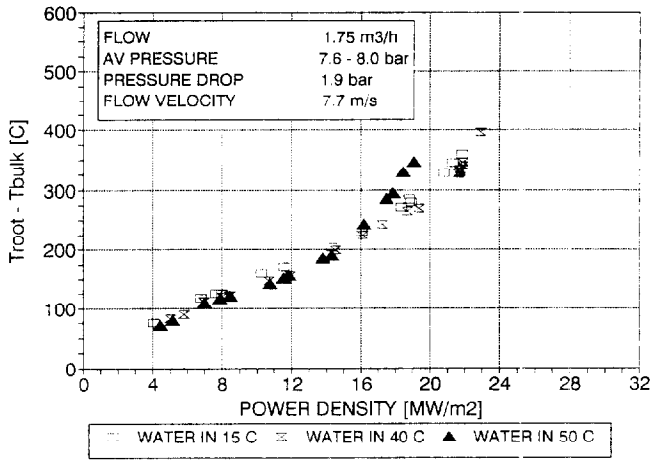

Fig. 18: Heat transfer in a vapotron with a water inlet temperature of 15, 40 and 50 °C and 7.5 bar.

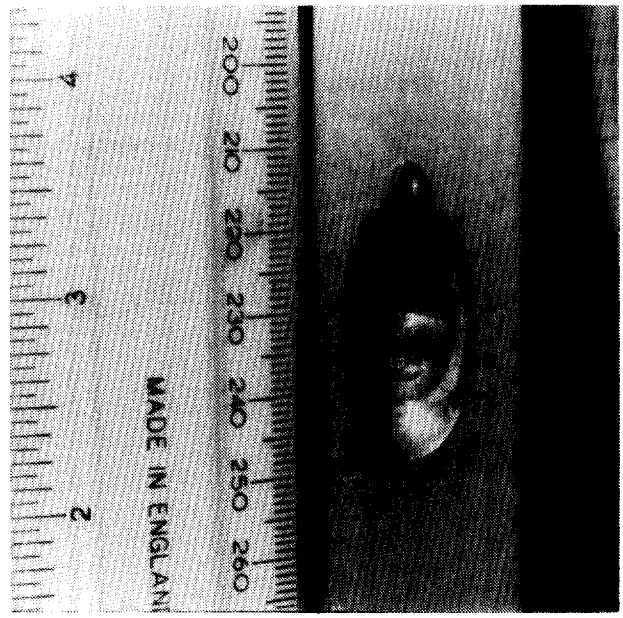

Fig. 16: Surface melting on a vapotron. Melting is between the fins, the fin periodicity of 6mm is clearly visible

critical heat flux in earlier scans. Fig. 15 shows a TC temperature trace at the critical heat flux of 14MW/m^2. The flow velocity was much lower (3m/s) with two elements in serial connection. The water temperature rise was 50°C in the second element, which suffered burnout. The temperature derivative in the copper is of the order of 125°C/s and it takes more than 3s between the loss of cooling and surface melting. Fig. 16 shows the melting after the burn-out. The periodicity of the fin structure and the local melting between the fins are clearly visible.

5.4. Velocity dependence of the heat transfer

A global heat transfer coefficient, defined as

$$h_{global}=(\text{power density})/(T_{wall}-T_{water})$$

can be used to describe the velocity dependences in the heat transfer as a function of the bulk water velocity. Data taken with test sections with a water channel height of 3, 6, and 8mm show that the heat transfer scales with the square root of the velocity, however, the scatter of the data is considerable. This

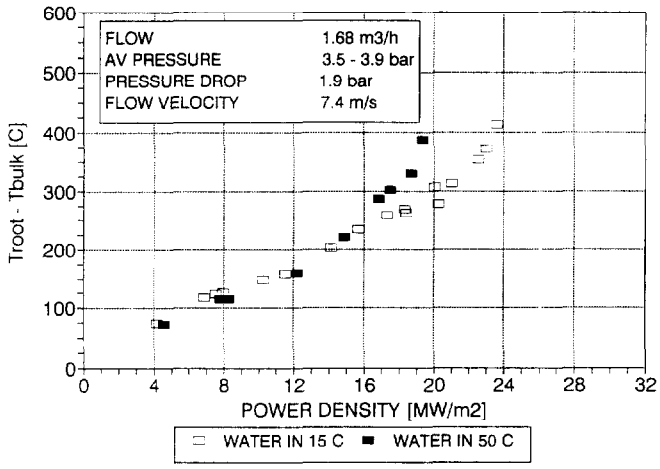

Fig. 19: Heat transfer in a vapotron with a water inlet temperature of 15. and 50°C and 3.5 bar

could indicate that resonant effects exist for the heat transfer at specific velocities.

5.5. Water pressure and subcooling

Power scans with 15. 40, and 50°C water inlet temperature and with 4 and 8 bar average pressure show (Fig. 18 & 19), that the heat transfer increases with water temperature at lower power densities and decreases with increasing water temperature at higher power densities. This again indicates, that the heat transfer deteriorates at higher power densities, when the water gets too hot. It appears that this wall temperature rise is correlated to water temperature rather than subcooling, as there is little influence from the water pressure.

6. Discussion of the heat transfer results

Fig. 14 shows clearly 3 different heat transfer regimes:

1 ***turbulent non boiling heat transfer up to 9 MW/m²***

2 ***boiling heat transfer between 9 and 16 MW/m². In this range there is no noise on the water pressure signal and***

3 ***boiling heat transfer range with reduced heat transfer and noise on the water pressure signal.***

A finite element analysis shows that we have to use an amplification factor ff of 1.35 in the modified Dittus Boelter correlation

$$Nu = 0.023 \times (ff) \times Re^{0.8} \times Pr^{0.33}$$

to describe the heat transfer before the onset of boiling. The bulk water velocity and the hydraulic diameter of the grooves between the fins are used in the Reynolds number Re. This suggests, that the vortices, created in the grooves between the fins, produce an average heat transfer similar to that in a pipe with the same hydraulic diameter but with 1.45 times the bulk water velocity . This is not unreasonable, as the momentum change in the vortex (circular flow) will reduce the width of the boundary layer and hence

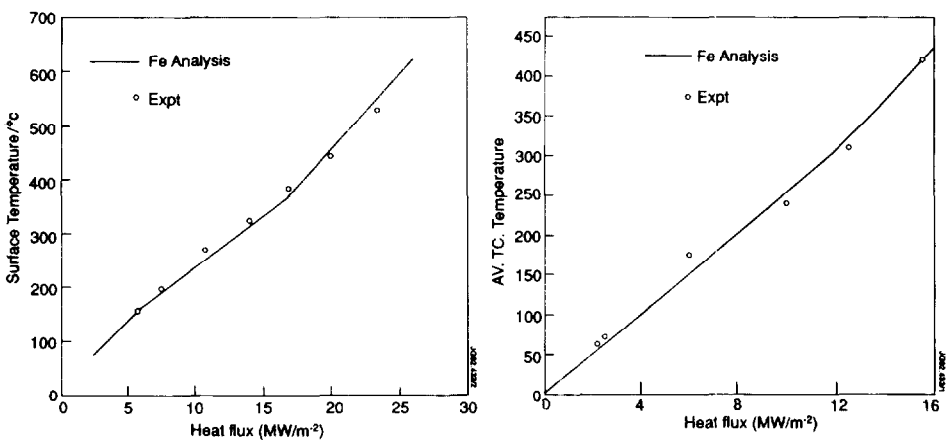

Fig. 21: Finite element analysis for bulk water flow velocities of 4 m/s, and 6.4 bar (left) and 11.5 m/s and 5.7 bar (right).

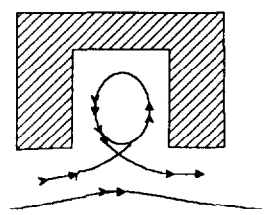

Fig. 20: Schematic vortex flow

improve the heat transfer (Reynold, Prandtl, and Karman analogy[7]). There must also be a sufficiently large exchange of cold water between the bulk flow and the water in the vortex. With this vortex picture in mind it is also not unreasonable to assume that we will get resonant effects at certain flow velocities, which would explain, why the heat transfer coefficient is not a monotonic function of the velocity.

With Thom's correlation in the nucleate boiling range and the Bergles Rosenhow correlation for temperatures above incipient boiling, we get the fits in Fig. 21 for a flow velocity of 4 and 11.5 m/s[8]. The agreement with the experimental data is quite good and demonstrates, that we do not have to assume a novel heat transfer mechanism to explain the heat transfer in a finned structure at higher velocities (>>3m/s).

This leads to the following basic model for a vapotron:

- The classical vapotron effect is only dominant at low flow velocities, where the ejection of steam from the grooves between the fins drives the heat transfer. In this range we see 10 - 20Hz oscillations in the water pressure which correspond to the ejection frequency.
- At high flow velocity the vortices are sufficiently violent to supply cold water into the grooves and the heat transfer is sufficiently large to avoid the formation of larger steam bubbles.

The advantages of a finned structure are:

- the increase of the heat transfer surface by the fins,
- the thermal inertia, which the cold fins provide in the case of a local burnout,
- turbulence is only created where it is needed to improve the heat transfer
- the water flow rate can be adjusted to the requirements by the width of the water channel.

7. Test Results from Beryllium tiles brazed onto CuCrZr Copper

Beryllium tiles have been brazed onto our standard vapotron element with a cross section of 500 x 27 mm^2. The beryllium tiles were 2 and 3 mm thick with different castellations. Sheer tests showed a strength of the brazed joint of 170 - 200 N/mm^2. The elements were, as foreseen in the divertor, rigidly fixed to a strong back which prevents movement due to thermal expansion. The test was carried out using modulated beams with on/off periods of equal lllength. The tiles were castellated into 6 x 6 mm^2, or 27 x 6 mm^2, or 27 x 27 mm^2 sections with the castellations penetrating either the full or half the thickness. Independent of the degree of castellation the tiles became detached when the power density exceeded 16 MW/m^2. This can be

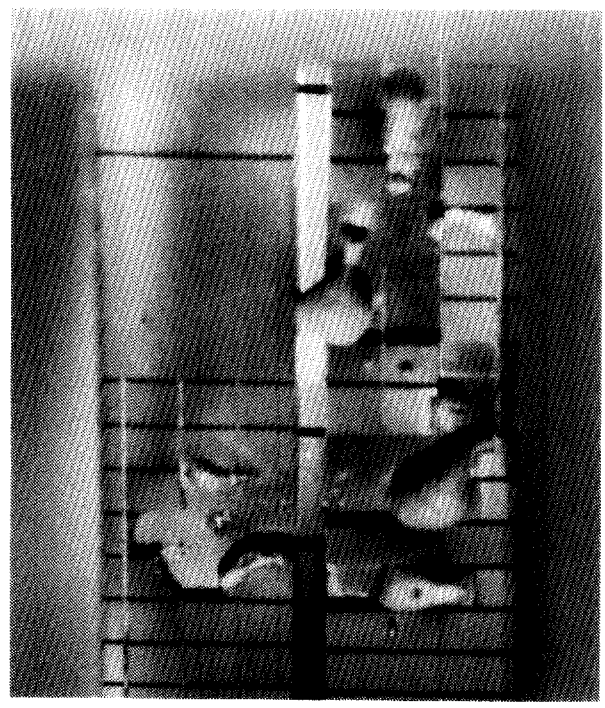

Fig. 22: Be tiles after the test

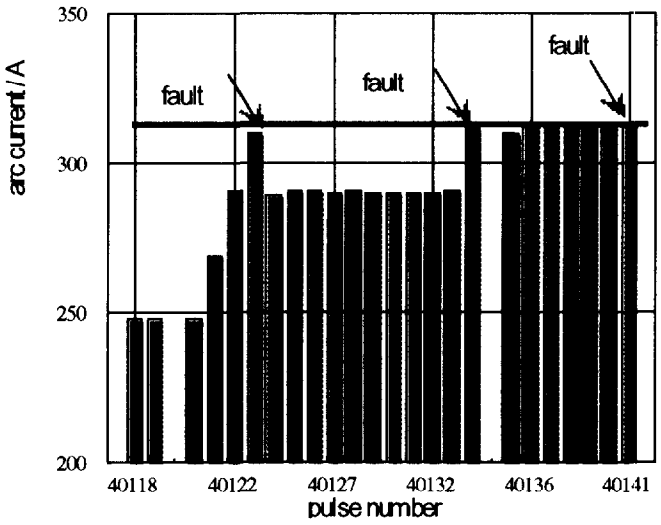

Fig. 23: Fault sequence for the B-Ag-18 braze. A fault develops, when the arc current exceeds 320 A. The arc current is proportional to the initial power density

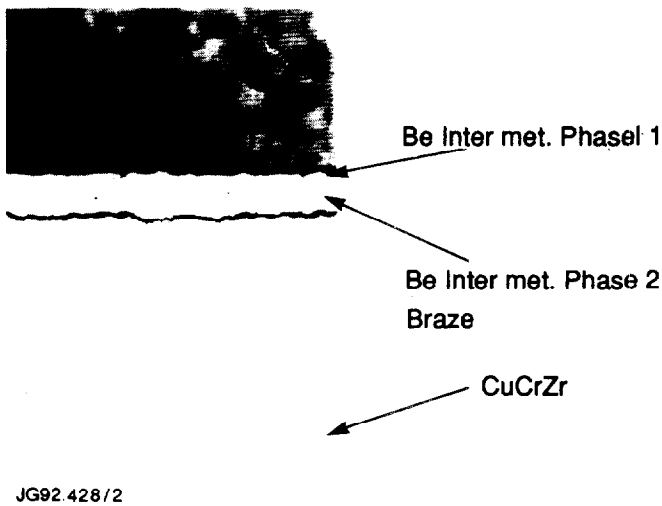

Fig. 24: Micrograph of the braze. Small cracks develop

clearly seen in Fig. 23. The faults are shown in Fig. 22, a photograph taken after the test.

Micrographs of the tiles after the test show (Fig. 24) that cracks develop in the inter-metallic layer between the braze and the Beryllium. This inter-metallic layer is very bridle (hardness 400 - 700 Vickers). Although the braze can withstand the average design loading of 12 MW/m^2 the safety margin is considered inadequate for an oscillating load. Alternative brazing procedures, which reduce the diffusion of Beryllium into the braze, are under investigation together with alternative bonding techniques such as plasma spaying, explosive bonding, or HIP-ing. Our tests confirmed, that it is indeed possible for the copper alloy to withstand the stresses generated by thermal expansion when the test element is rigidly supported.

References:

[1]) P-H Rebut, Magnetic confinement Fusion: Recent Results at JET and Plans for the Future, JET-P(92)21, (preprint of an invited talk 3rd Eur. Part. Acc. Conf., Berlin, Germany, 24th - 28th March 1992 and M Huguet, Design of the JET Pumped Divertor, JET-P(91)51, preprint of a paper presented to the 14th Symp. on Fus. Eng., San Diego, USA, 30 Sept - 3rd Oct. 1991

[2]) CH Beutheret, Perfectionnements aux dispositifs d'echange de chaleur entre une paroi et un liquide, French patent No 1, 502, 797, 16th Oct. 1967

[3]) H D Falter, Power Loading Tests of the JET Pumped Divertor Plates, Proceedings of the 16th Symp on Fus Techn, London U.K., 3-7 Sept. 1990, ISBN 0 444 88508 0, Elsevier Science Publishers B.V. 1991

[4]) E Deksnis, Solid Beryllium Tiles for the JET pumped Divertor, this conference, paper1739-14

[5]) AGA Thermovision 782, AGA Infrared Systems AB, S 18211 Danderyd, Sweden

[6]) Type 7201, Fisher Controls Ltd, Tylors Works, Victoria Road, Burgess Hill, Sussex RH15 9LJ, U.K.

[7]) M N Özisik, Heat Transfer a basic approach, McGraw-Hill Book Company, New York, 1985

[8]) C B Baxi, A Model for Analytical Performance Prediction of Hypervapotron, To be presented to 5 Int Topical Meeting on Nuclear Reactor Thermal Hydraulics, Salt Lake City, USA, 21-24 Sept. 1992

200
210
220
230
240
250
260
MADE IN ENGLAN
2
3
4

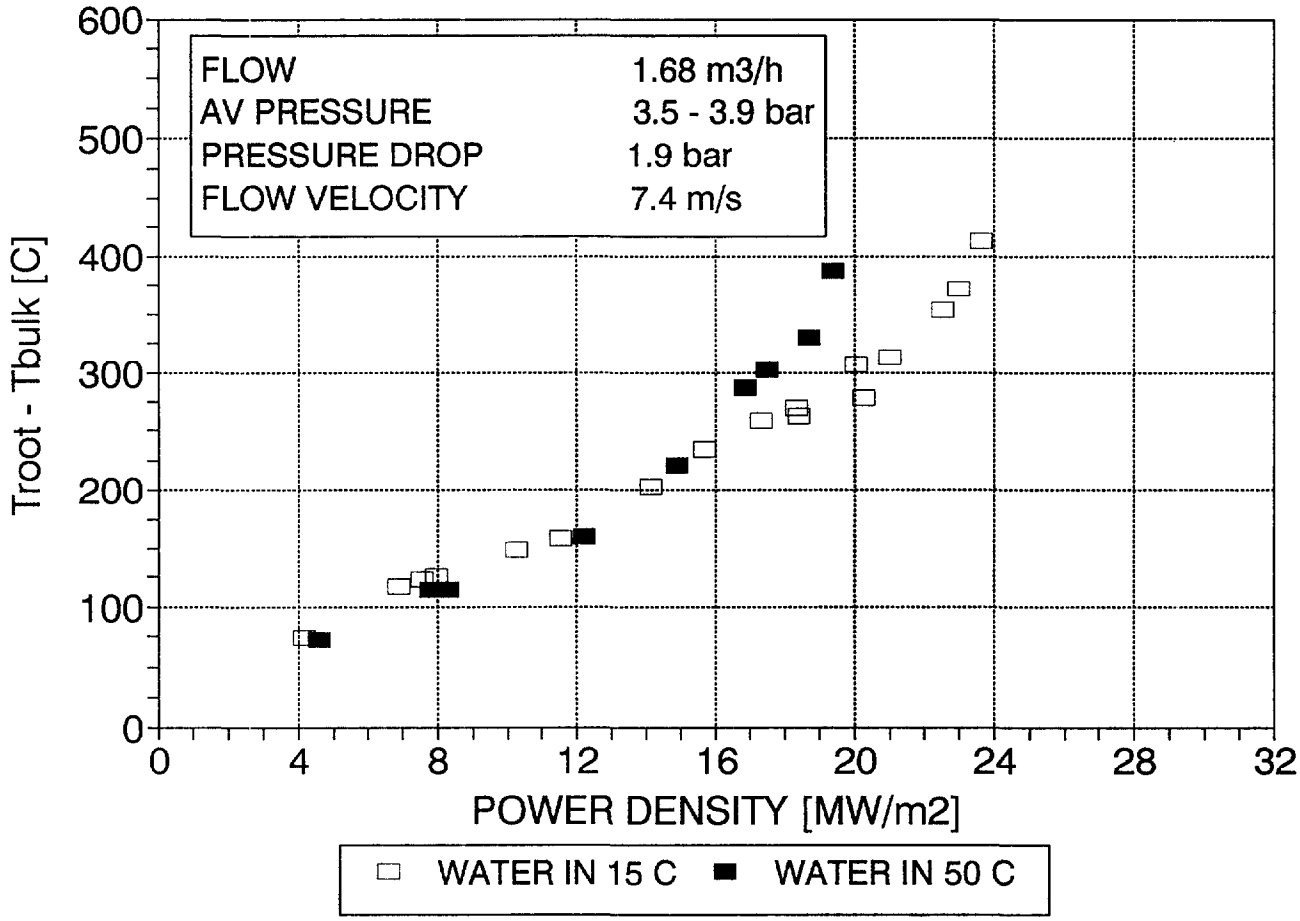
FLOW 1.68 m3/h
AV PRESSURE 3.5 - 3.9 bar
PRESSURE DROP 1.9 bar
FLOW VELOCITY 7.4 m/s
Troot - Tbulk [C]
600
500
400
300
200
100
0
0
4
8
12
16
20
24
28
32
POWER DENSITY [MW/m2]
WATER IN 15 C
WATER IN 50 C

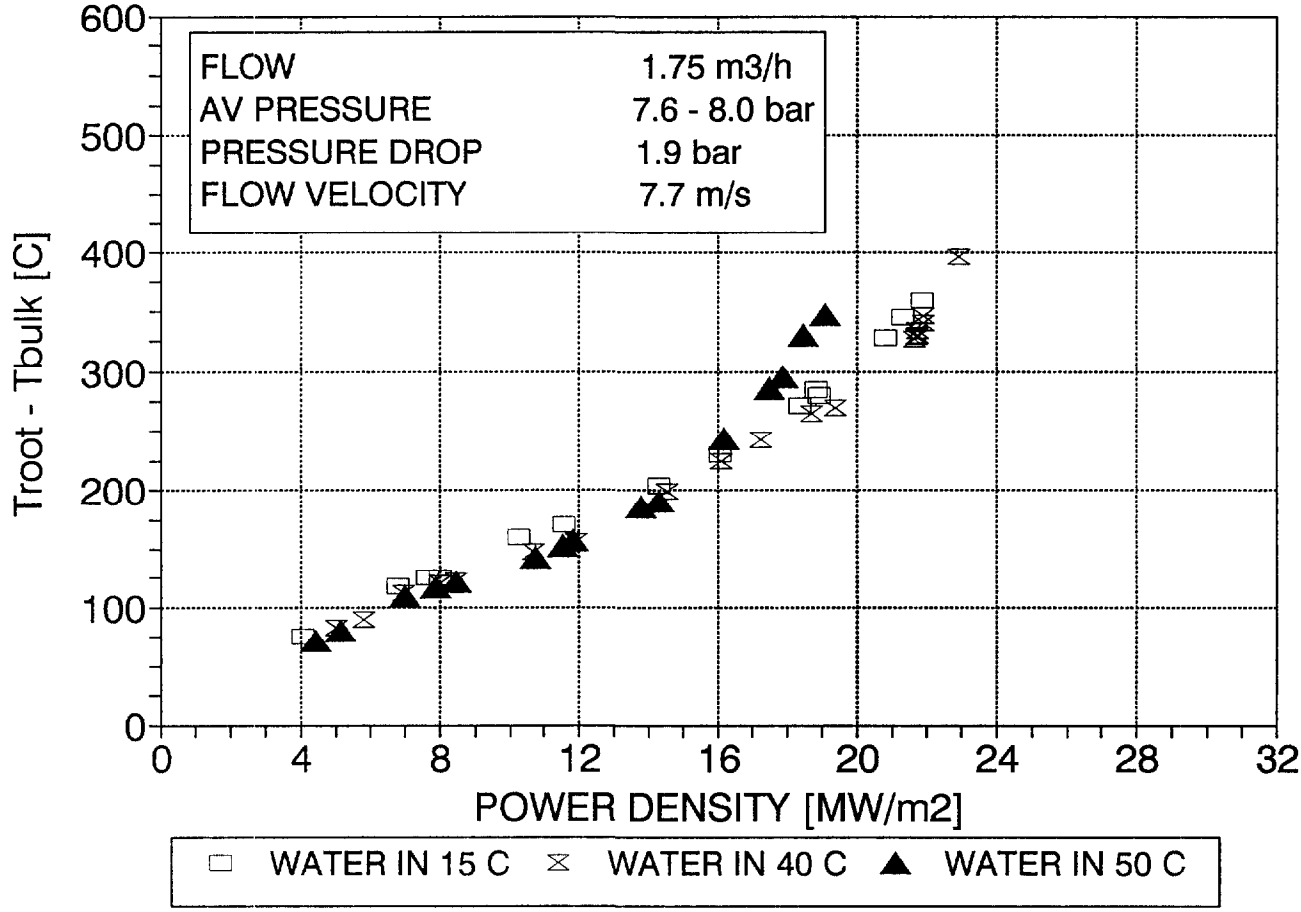
FLOW 1.75 m3/h
AV PRESSURE 7.6 - 8.0 bar
PRESSURE DROP 1.9 bar
FLOW VELOCITY 7.7 m/s
Troot - Tbulk [C]
600
500
400
300
200
100
0
0
4
8
12
16
20
24
28
32
POWER DENSITY [MW/m2]
WATER IN 15 C
WATER IN 40 C
WATER IN 50 C

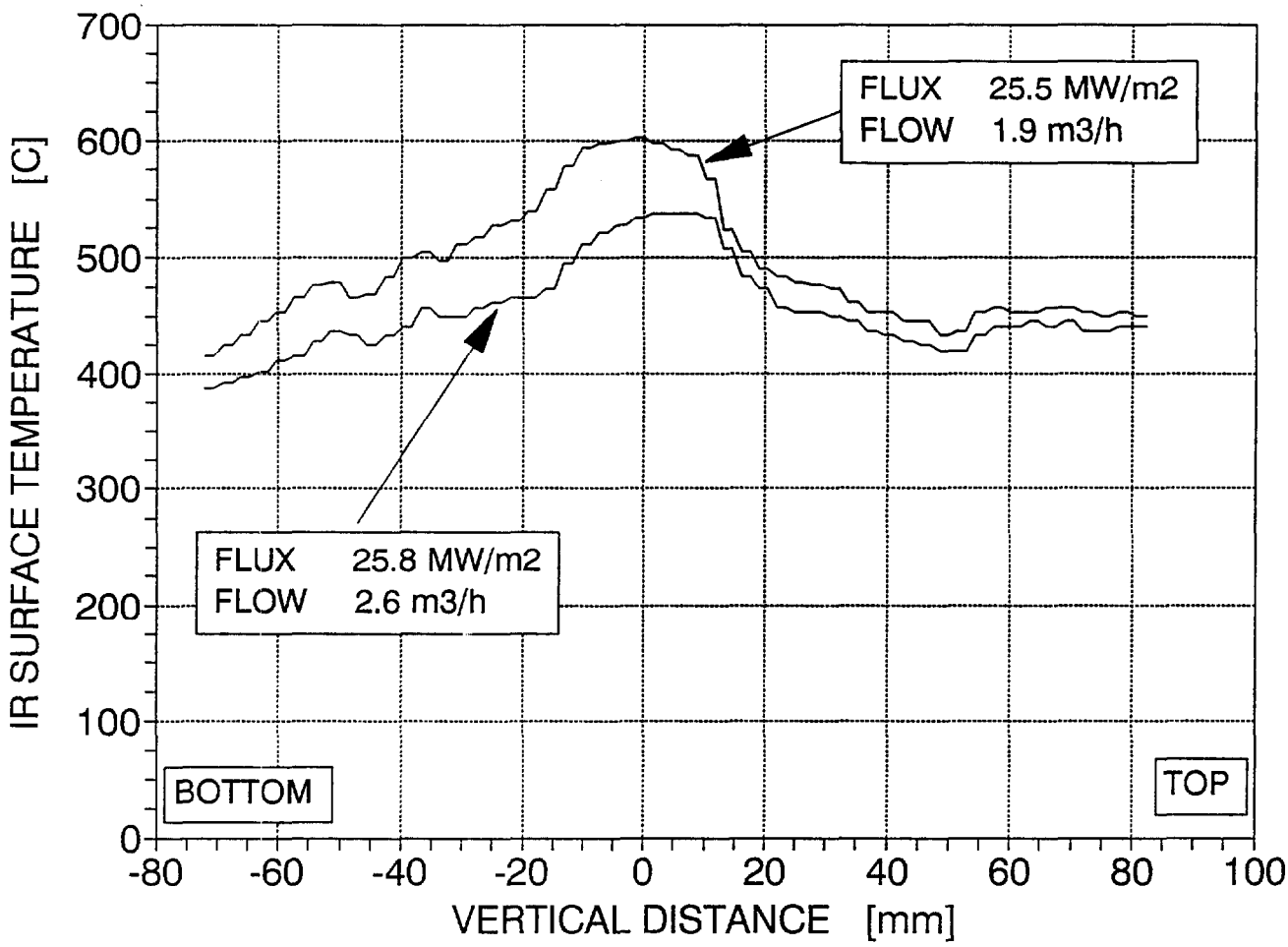
IR SURFACE TEMPERATURE [C]
700
600
500
400
300
200
100
0
-80
-60
-40
-20
0
20
40
60
80
100
VERTICAL DISTANCE [mm]
FLUX 25.5 MW/m2
FLOW 1.9 m3/h
FLUX 25.8 MW/m2
FLOW 2.6 m3/h
BOTTOM
TOP

Thermal test results of the JET divertor plates

H D Falter [1], H Altmann [1], Ch Baxi [2] G H Deschamps [1], R S Hemsworth [3], D Martin [1], P Massmann [1]

[1]) JET Joint Undertaking, Abingdon, OXON OX14 3EA, England,
[2]) GENERAL ATOMICS, San Diego, Ca, 92186-9784,USA
[3]) DFRC Tore Supra, CEN Cadarache, F-13108 St Paul Lez Durance (Cedex), France

1. ABSTRACT

The actively cooled version of the JET divertor plates use a finned structure as heat exchange surface between the copper alloy base plate and the cooling water (hypervapotron). The turbulence created by the fin structure gives a remarkably good heat transfer even before the onset of boiling. The boiling heat transfer is stabilised by the colder fin structure. Finite element calculations confirm that the heat transfer can be explained by turbulent boiling heat transfer.

Power densities of up to 25MW/m^2 can be removed with a pressure drop of 4bar per meter. Beryllium tiles brazed to the CuCrZr base plate can withstand a pulsed power loading of up to 16 MW/m^2. Limiting in strength is the intermatallic layer between the braze and the Beryllium tile. The test sections, mounted rigidly against a strong back, withstood the stress caused by thermal expansion.

2. INTRODUCTION.

The JET Joint European Torus[1] in Culham U.K. operates in a pulsed mode with a pulse duration of up to 60s. The plasma is confined by magnetic fields and heated by the current in the plasma (up to 7 MA). Up to 40 MW of additional power can be supplied by the plasma heating systems. The energy confinement time is of the order of 1s. The exhausted power is absorbed in specially designed dumps. Impurities, released from the dump can lead to radiative losses and to dilution of the plasma. Both effects increase with the atomic number Z of the impurity. To minimise plasma contamination, low surface temperatures of the dump plates and a dump surface material with a low atomic number, such as Beryllium or Graphite, are beneficial. Any misalignment of the dump plates will cause localised hot spots and must be avoided.

A so-called "divertor", which separates the dump area from the plasma, is at present being installed into the JET machine. The strike area between the plasma exhaust flux and the dump plates will be swept with a frequency of 4 Hz, thus reducing the peak heat flux of 60 MW/m^2 to a time average heat flux of 12 MW/m^2. In this paper we report on thermal tests of the water cooled base plates made from CuCrZr with finned internal surfaces (Vapotron)[2] and on tests of base plates with Be tiles brazed onto the exposed surface. In a previous paper [4][3] we have reported the results of experimental studies of the heat transfer of vapotron structures. It was found that the detailed geometric structure has little influence but the velocity of the cooling water was of major importance. The classical vapotron effect, where the steam formation in the grooves and its ejection

provides the driving force of the heat exchange, is only seen at low velocities. With increasing velocity, the turbulence created by the fin structure appears to dominate the heat transfer. This observation led to the development of a test section with a reduced water channel width and reduced fin height. The heat transfer characteristics of this element is covered in this report.

3. Divertor Dump Plates

The divertor dump is made up from 48 modules to form a complete toroidal ring. The bottom section is the actual dump and will, in a second operation phase, consist of 8 individual 900 mm long actively cooled dump plates per module (Fig. 1). The tiles at the sides and initially at the bottom are made from solid beryllium with inter pulse cooling[4]. The actively cooled dump plates are rigidly connected to a strong back to prevent movement and distortion due to thermal expansion. The cross section of each dump plate increases along the length from 27 x 19 mm to 36 x 19 mm (toroidal dump). The water flow rate is 0.5l/s per actively cooled element. The heat transfer between the dump plate and the water is via a finned surface. The height of the water channel defines the ratio between flow rate and velocity and can be adjusted to the specific requirements to optimise the water circuit. (Fig. 2) The water channel in the JET divertor plates is tapered to maintain a constant flow velocity of 7m/s.

4. Test Facility

All the tests in this report have been performed in the JET Neutral Beam Test Bed, a 10MW, 160 kV beam line set up initially to commission the JET neutral beam injectors

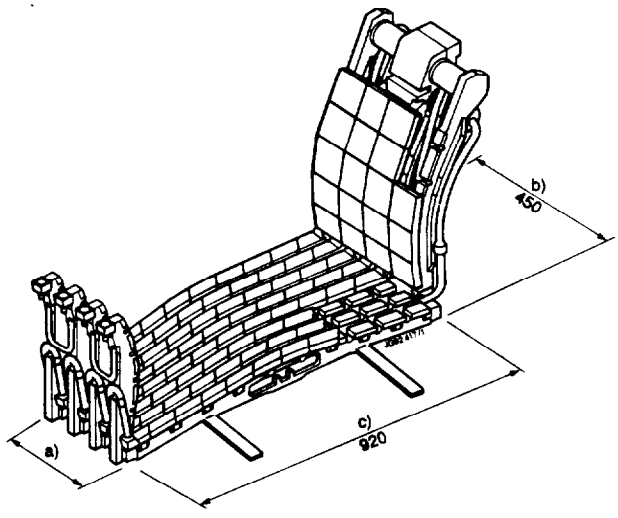

Fig. 1: Module assembly of the JET divertor. Initially all tiles are inertial (interpulse cooled). Later the bottom tiles will be actively cooled elements as descibed here.

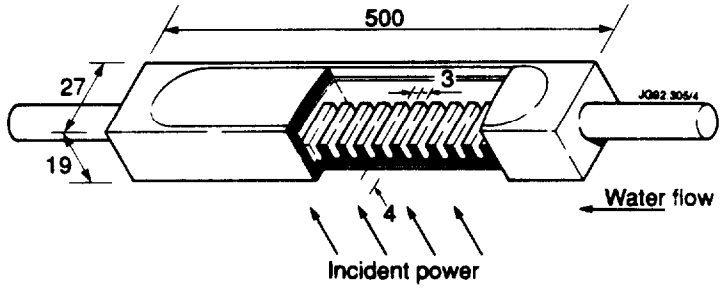

Fig. 2: Vapotron schematic. The heat transfer into the water is through a finned surface. The water channel width can be designed to match the flow requirements.

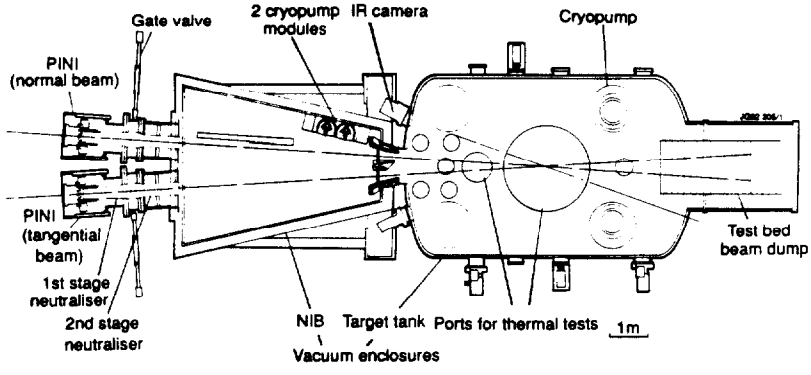

Fig. 3 : Schematic of the main beam line of 12m length. Tests are carried out in the Target Tank, 7 - 8 m from the beam source.

Table 1:	TB specification
heat source	ion beam
pulse duration	20s
max. power	2 x 4 MW
max. power density	100MW/m^2 per beam
duty cycle	1 : 30
volume	90m^3
access ports	up to 1500 mm i.d.
vacuum pumping speed	10^6 l/s for Hydrogen
Cooling loop capacity available for tests:	
water flow rate and pressure head	20 l/s (8 bar) & 100 l/s (4.5bar)
return water pressure	2 bar

(Fig. 3). The main parameters of the Test Bed are shown in Table 1. Heat transfer tests are carried out in the Target Tank. Samples with Beryllium are tested in a second smaller beam line, the so called Beryllium test rig (Fig. 4), to avoid contamination of the main beam line with toxic Beryllium dust.

4.1. Tests with Beryllium

The Beryllium test rig is a small beam line with a volume of approximately 1 m^3. The whole tank is operated at the pressure required in the plasma source to produce an arc (0.2 - 0.3 Pascal). This reduces the requirement for vacuum pumping speed considerably to less than 1000l/s. The ion source used is a standard JET source with a reduced extraction area. Power supplies, control & data acquisition, and the cooling loop of the main test Bed are shared with the main beam line.

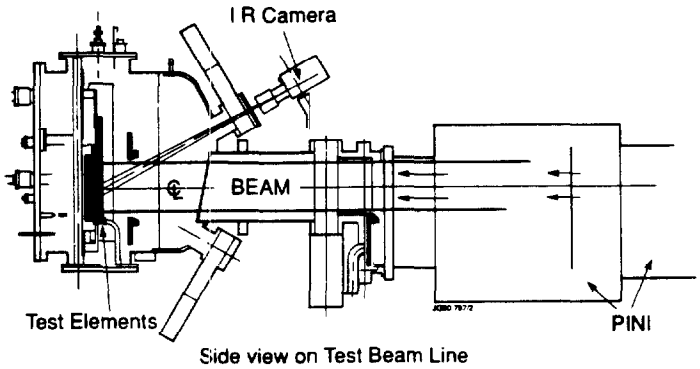

Fig. 4: Side view of the beam line for tests with Beryllium components. The distance between beam source and target is 2m, the volume of the beam line is 1 m^3.

4.2. Instrumentation

4.2.1. Surface temperature

The surface temperature of the test panel is measured with an AGA IR camera[5]. Before and after a test the camera is calibrated against the CrAl thermocouples in the panels. This is done by heating the uncooled panel with the ion beam. The output of the IR camera is then calibrated against the thermocouple temperature. This procedure guarantees, that the panel is in thermal equilibrium.

4.2.2. Panel temperature

Bare wire CrAl thermocouples are percussion welded into 1.7 mm holes. The hot junction is normally 2mm below the exposed surface. The thermocouple output is sampled with a rate of app. 40 Hz. Assuming one dimensional heat conduction, we can calculate the surface temperature and the temperature of the water-wall interfaces from the TC temperature.

4.2.3. Water flow calorimetry

Water flow is measured using Taylor turbine flowmeters[6] installed in the return line of each water channel. The water exit temperature is measured by sheathed CrAl thermocouples sampled at a rate of 6 Hz. The signal level before the pulse is used as a base line.

4.2.4. Beam profile

The horizontal and the vertical beam profiles are measured using drive-in inertial calorimeters. The vertical profile is additionally measured using a calorimeter strip installed behind the gap between the test sections.

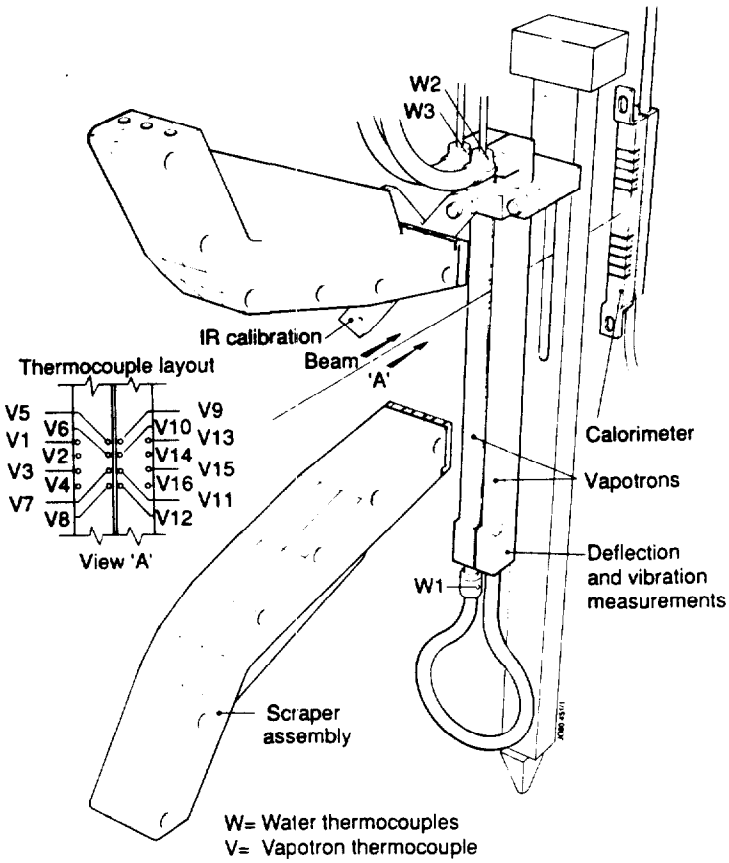

Fig. 5: Test setup in the Target Tank: two test sections are mounted side by side with a 2mm gap and a vertical calorimeter behind the gap. Thermocouples are grouped around the centre position.

source and test section is of the order of 2m and the beam profile has a larger flat top area of approximately 100 x 40 mm² (vertical x horizontal).

4.4. Test Rig and test samples

4.4.1. Large test facility

Two elements of 27mm width each are installed side by side with a nominal gap of 2mm (Fig. 5). Water flow can be either serial, (as shown in Fig. 5), or parallel. The vertical beam width is limited to 175 mm by two scrapers. The test sections were vapotrons with 500 x 27 x 19 mm³. The internal fin structure was as detailed in Table 2. Thermocouples are installed in the side walls with a distance of 2mm from the surface exposed to the beam. Alongside a vapotron test section we have also tested a swirl tube

This latter diagnostics is used for relative measurements only, because the width of the gap between the elements is not well defined.

4.3. Ion Beam

4.3.1. Parameters:

The JET Test Bed can be operated with Hydrogen, Deuterium, or Helium Beams. In Hydrogen or Deuterium, typically 60 - 80% of the power is in the full energy component (ions accelerated as H^+) and the rest in the half and third energy component (ions accelerated as H_2^+ or as H_3^+). Roughly 50% of the extracted ion beam is converted into neutral atoms due to charge-changing collisions after acceleration. The beam can be 100% amplitude modulated with a minimum off period of 30ms and a minimum on period of approximately 3 ms. This modulation has been used to simulate the sweeping of the plasma strike point over the dump plates.

4.3.2. Beam profile

The distance between the beam source and the test section is 7m in the large test facility. The beam has essentially a gaussian shape with a small (30mm) flat top in the vertical plane and with scraped edges (±75mm) in the horizontal plane. The 1/e width is of the order of 100 mm. In the Be test rig the distance between beam

Table 2: vapotron dimensions

fin height	4 mm
fin width	3mm
groove between fins	3mm
water channel height	3mm

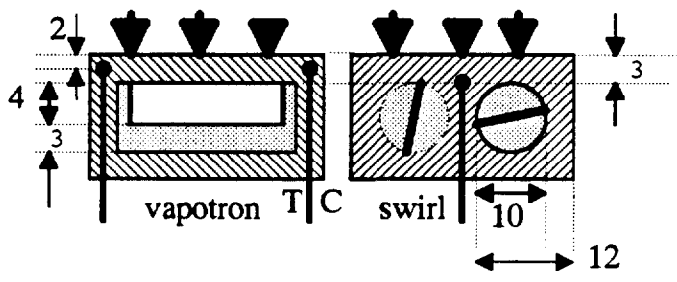

Fig. 6: Schematic of the test sections

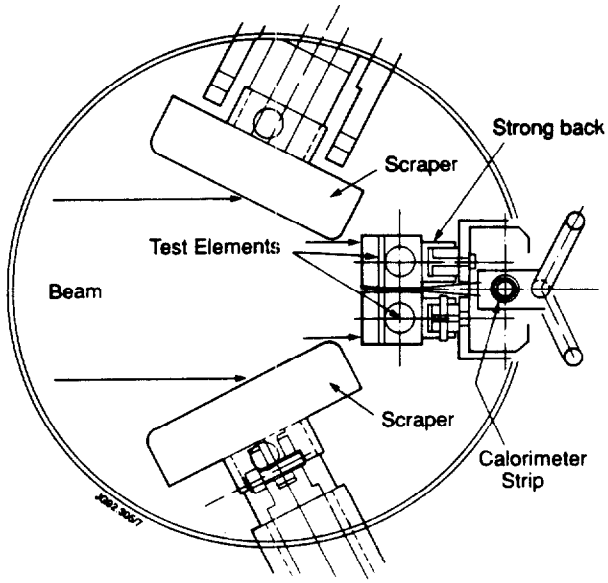

Fig. 7: Test set-up in the Beryllium test rig: The outer vertical edges of the elements are shielded by scrapers. The sections are rigidly mounted against a strong back. A calorimeter is installed behing the gap between the two elements.

section having the same external dimensions and using parallel connection for the coolant flow. The swirl tube section had two drillings of 10mm each with a twisted tape of twist ratio 2. Thermocouples where installed in the side wall, 3mm from the exposed surface. Fig 6 shows a schematic of both test sections.

4.4.2. Be Test Rig

The test sections are rigidly fixed against a strong back. The exposed area is 200 x 48mm². The outer edges of both vapotrons are behind the scrapers (Fig. 7).

5. Experimental results

5.1. Vapotron Heat Transfer

Power scans have been done with a vapotron and a swirl tube section installed side by side. The surface temperature of the test sections are shown in Fig.'s 8 and 9 as a function of the power density for two flow rates. The main effect of the higher flow rate is, in both cases, the extension of the operating range to higher power densities without excessive rise of the surface temperature. At power densities below 20MW/m², the surface temperature is the same for both flow rates. If anything, both panels are marginally colder at a given power density with the lower flow rate, indicating, that the gain in heat transfer with velocity is compensated by the higher viscosity due to the lower water

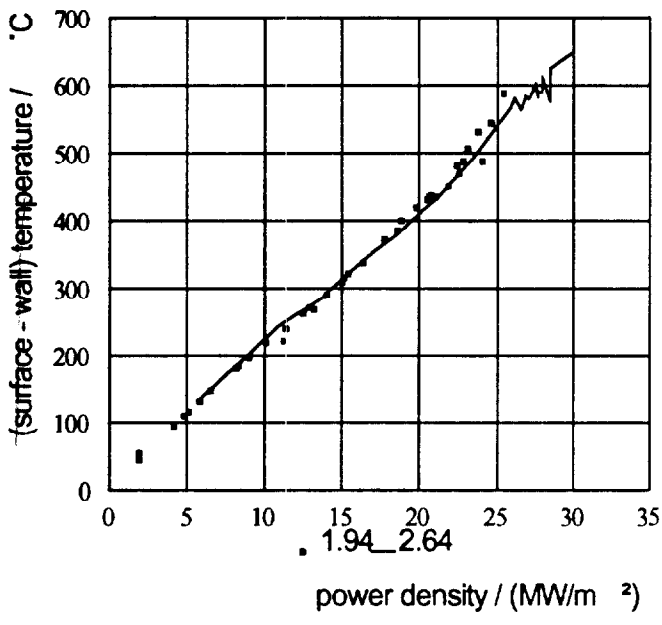

Fig.. 8: Vapotron surface temperature for water flow rates of 1.94 & 2.64 m³/h (8.5 & 11.6 m/s velocity)

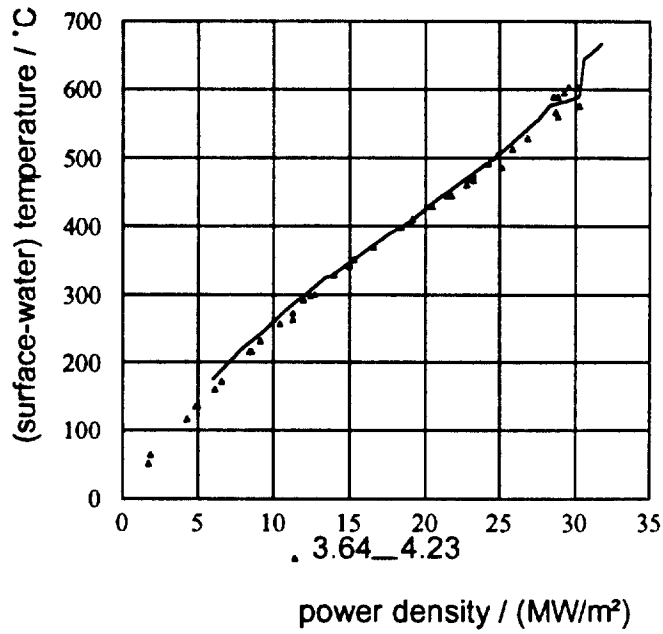

Fig. 9: Swirl tube surface temperature for water flow rates of 3.64 & 4.23 m³/h (7.4 & 8.6 m/s velocity)

temperature. In the case of the vapotron, the flow rates of 1.94 and 2.64m³/h correspond to a bulk water velocity of 8.4 and 11.5 m/s. The range of interest for the JET divertor is for a surface temperature up to 350 °C. This corresponds to a power density of approximately 17MW/m². At the low flow rate the highest absorbed energy was 0.509 MW with a pulse length of 4.86s.

5.2. Comparison Vapotron - swirl tube

The surface temperatures of the vapotron and the swirl tube section are almost identical (Fig. 10). The swirl tube has a slightly higher surface temperature up to 20MW/m². Above this power density the situation is reversed. The total power absorbed by both sections was almost identical. The higher temperature of the swirl tube section could again be explained (at least partially) by the higher flow rate and therefore lower water temperature. In the case of the swirl tube section we actually achieved the critical heat flux of 30MW/m² at the lower flow rate.

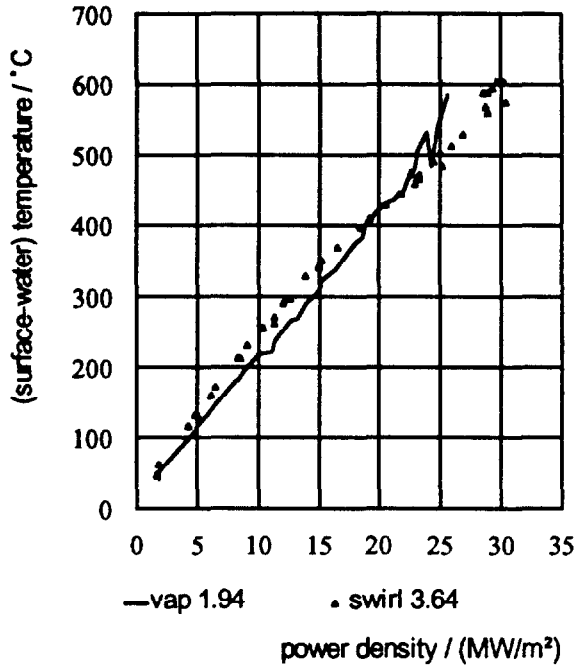

Fig. 10: Comparison vapotron (line) & swirl tube (symbols) for flow rates of 1.94 (vapotron) and 3.64 m³/h (swirl tube)

Table 3: Comparison of vapotron and swirl tube data: Δp: pressure drop at the quoted flow rate, ΔT_w: water temp. rise in °C, pump factor: flow x pressure (in Watt).

#40958	flow m³/h	$\frac{\Delta p}{bar}$	$\frac{power}{MW/m^2}$	ΔT_w	pump factor in Watt
vapotron	1.94	2.2	25.5	46.3	119
swirl tube	3.64	3.9	26.9	26	395

5.2.1. Pressure

Under operating conditions, vapotron and swirl tube compare as shown in table 3: The swirl tube needs nearly twice the flow and requires more than three times the pumping power. The vapotron produces twice the noise level at the water outlet compared to the swirl tube (Fig. 11) (actually, the noise levels at the in- and outlet of the swirl tube are roughly of the same magnitude and might both be created by the vapotron).

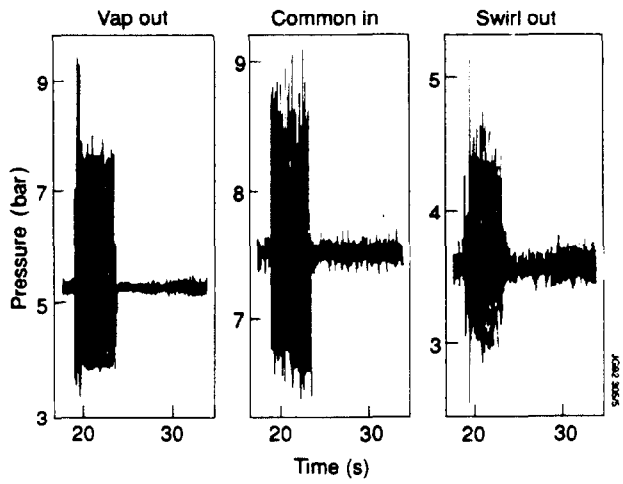

Fig. 11: Noise on the water pressure signals in bar for a high power pulse (data in table 3). Left: vapotron outlet pressure, middle: common inlet pressure, right: swirl tube outlet pressure

5.2.2. Surface temperature

Fig. 12 shows vertical profiles of the vapotron surface temperature for two pulses with 25.5 and 25.8MW/m². The water is flowing from top to bottom. The centre is clearly overheating in both cases and the profile is unsymmetrical, shifted in the direction of the water flow.

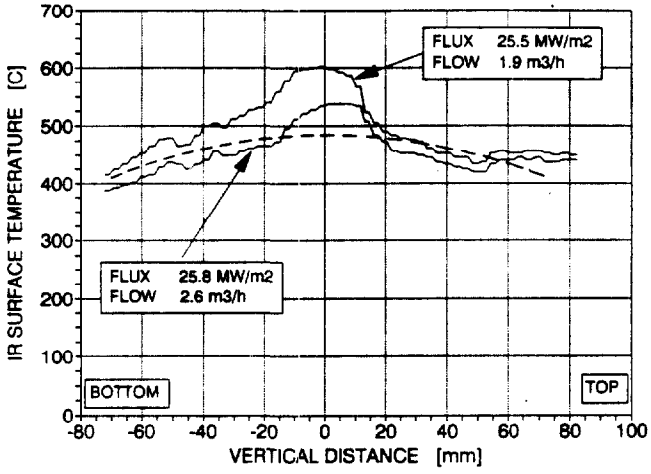

Fig. 12: Vertical profile of the vapotron surface temperature from the IR camera for a power density of 26MW/m². The dashed line is an eye fit to estimate the overheating

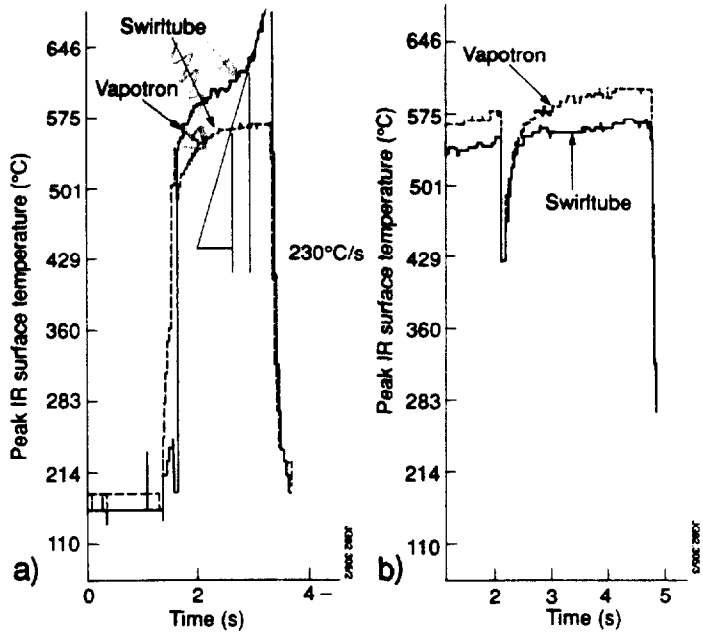

Fig. 13: Peak surface temperature from the IR camera, a) for the swirl section at critical heat flux (29.5MW/m²), and b) for the highest heat flux on the vapotron at 1.94m³/h for the pulse in table 3

This indicates insufficient subcooling. Increasing the flow rate from 1.9 to 2.6 m³/h reduces mainly the overheating in the centre and at the downstream end. This explains, why the vapotron shows higher surface temperatures with the low flow rate at high power densities in Fig. 8. The overheating is of the order of 100°C, as indicated by the dashed line in Fig. 12. In the case of the swirl tube we had two cases, where the temperature was running away. Fig. 13a shows the temperature rise measured with the IR camera at the hottest section of each element. The power density was 29.5 MW/m², the flow rate 3.58m³/h for the swirl tube and 27.5MW/m² and 2.64m³/h for the vapotron. The temperature rise at the surface of the swirl section is of the order of 230°C/s. Fig. 13b shows the vapotron surface temperature for the highest power density with the lower flow rate (25.5MW/m² and 1.94m³/h) together with the surface temperature of the swirl tube (26.9MW/m² and 3.68m³/h). The vapotron is clearly hotter, but still stable.

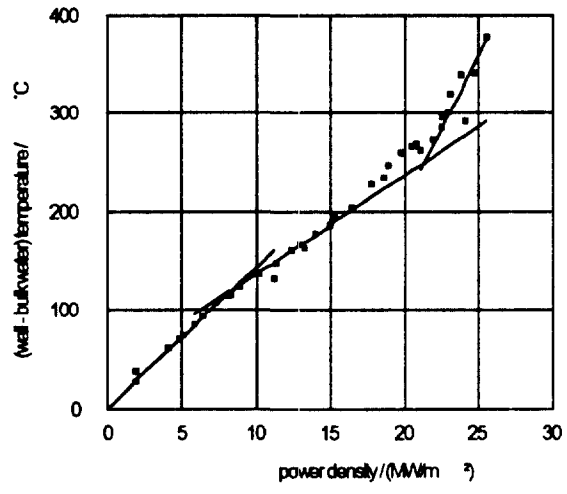

Fig. 14: Temperature difference in the vapotron across the heat exchange surface (wall - bulk water) for a flow of 1.94 m³/h

5.3. Vapotron at critical heat flux

As mentioned in 5.1, we did not take the vapotron to burnout, as the surface temperature at the high power level is well above that which is acceptable to us for other reasons. At power densities above 17MW/m² we can clearly see an excessive temperature rise in Fig. 14 of up to 100°C at the highest power density. This excessive temperature only occurs in the area with the peak power density (Fig. 12). The amount of overheating derived from Fig. 12 and 14 is identical. It is assumed, that the overheating is due to a locally over-critical heat flux which is stabilised by heat conduction into the fins. We have tested vapotrons to the

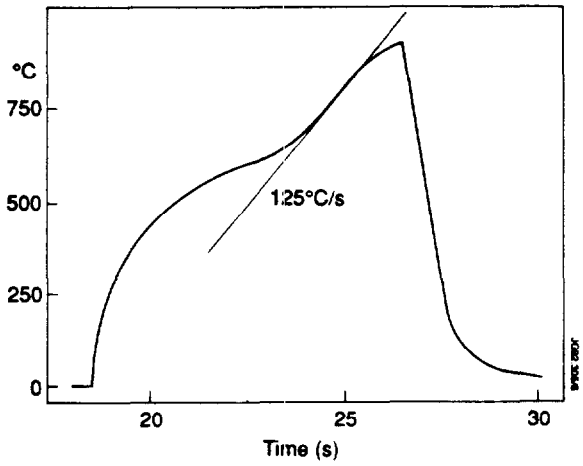

Fig. 15: TC temperature trace for a vapotron above the critical heat flux

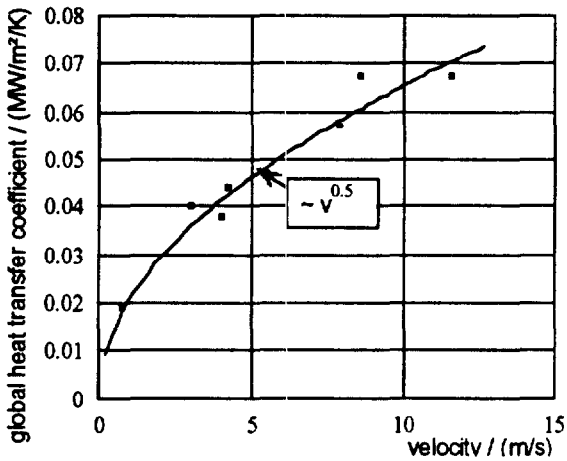

Fig. 17: Velocity dependence of the heat transfer in vapotrons with 4 mm fin height

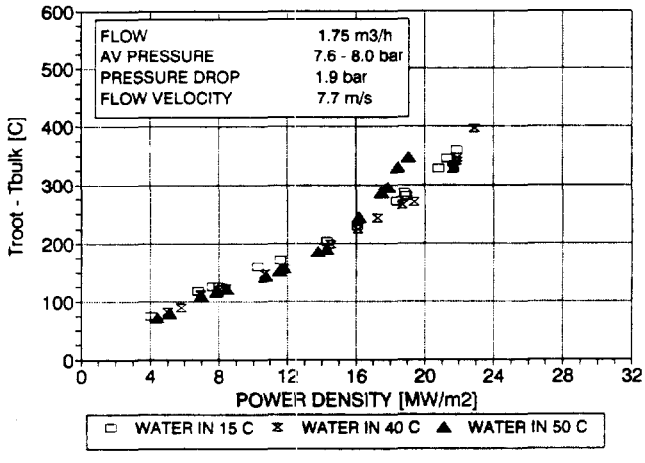

Fig. 18: Heat transfer in a vapotron with a water inlet temperature of 15, 40 and 50°C and 7.5 bar.

Fig. 16: Surface melting on a vapotron. Melting is between the fins, the fin periodicity of 6mm is clearly visible

critical heat flux in earlier scans. Fig. 15 shows a TC temperature trace at the critical heat flux of 14MW/m^2. The flow velocity was much lower (3m/s) with two elements in serial connection. The water temperature rise was 50°C in the second element, which suffered burnout. The temperature derivative in the copper is of the order of 125°C/s and it takes more than 3s between the loss of cooling and surface melting. Fig. 16 shows the melting after the burn-out. The periodicity of the fin structure and the local melting between the fins are clearly visible.

5.4. Velocity dependence of the heat transfer

A global heat transfer coefficient, defined as

$$h_{global}=(\text{power density})/(T_{wall}-T_{water})$$

can be used to describe the velocity dependences in the heat transfer as a function of the bulk water velocity. Data taken with test sections with a water channel height of 3, 6, and 8mm show that the heat transfer scales with the square root of the velocity, however, the scatter of the data is considerable. This

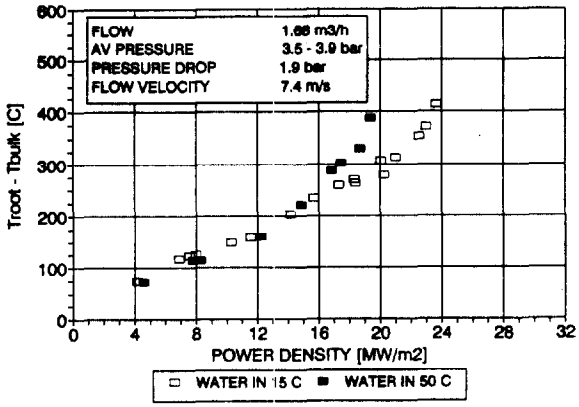

Fig. 19: Heat transfer in a vapotron with a water inlet temperature of 15. and 50 °C and 3.5 bar

could indicate that resonant effects exist for the heat transfer at specific velocities.

5.5. Water pressure and subcooling

Power scans with 15. 40, and 50°C water inlet temperature and with 4 and 8 bar average pressure show (Fig. 18 & 19), that the heat transfer increases with water temperature at lower power densities and decreases with increasing water temperature at higher power densities. This again indicates, that the heat transfer deteriorates at higher power densities, when the water gets too hot. It appears that this wall temperature rise is correlated to water temperature rather than subcooling, as there is little influence from the water pressure.

6. Discussion of the heat transfer results

Fig. 14 shows clearly 3 different heat transfer regimes:

1 ***turbulent non boiling heat transfer up to 9 MW/m²***

2 ***boiling heat transfer between 9 and 16 MW/m². In this range there is no noise on the water pressure signal and***

3 ***boiling heat transfer range with reduced heat transfer and noise on the water pressure signal.***

A finite element analysis shows that we have to use an amplification factor ff of 1.35 in the modified Dittus Boelter correlation

$$Nu = 0.023 \times (ff) \times Re^{0.8} \times Pr^{0.33}$$

to describe the heat transfer before the onset of boiling. The bulk water velocity and the hydraulic diameter of the grooves between the fins are used in the Reynolds number Re. This suggests, that the vortices, created in the grooves between the fins, produce an average heat transfer similar to that in a pipe with the same hydraulic diameter but with 1.45 times the bulk water velocity. This is not unreasonable, as the momentum change in the vortex (circular flow) will reduce the width of the boundary layer and hence

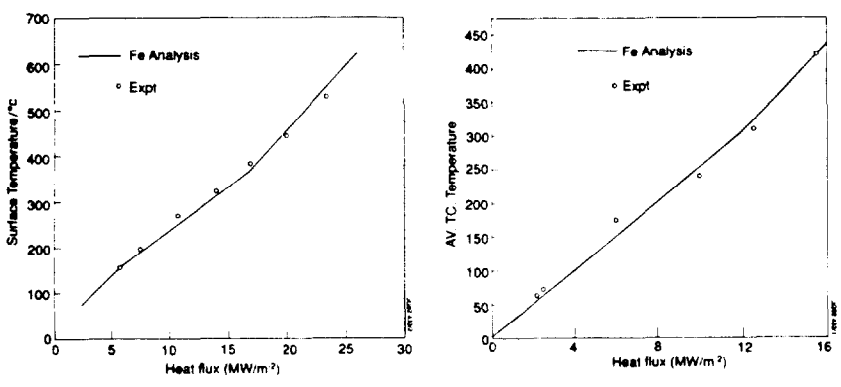

Fig. 21: Finite element analysis for bulk water flow velocities of 4 m/s, and 6.4 bar (left) and 11.5 m/s and 5.7 bar (right).

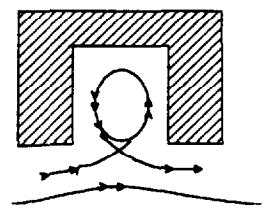

Fig. 20: Schematic vortex flow

improve the heat transfer (Reynold, Prandtl, and Karman analogy[7]). There must also be a sufficiently large exchange of cold water between the bulk flow and the water in the vortex. With this vortex picture in mind it is also not unreasonable to assume that we will get resonant effects at certain flow velocities, which would explain, why the heat transfer coefficient is not a monotonic function of the velocity.

With Thom's correlation in the nucleate boiling range and the Bergles Rosenhow correlation for temperatures above incipient boiling, we get the fits in Fig. 21 for a flow velocity of 4 and 11.5 m/s[8]. The agreement with the experimental data is quite good and demonstrates, that we do not have to assume a novel heat transfer mechanism to explain the heat transfer in a finned structure at higher velocities (>>3m/s).

This leads to the following basic model for a vapotron:

- The classical vapotron effect is only dominant at low flow velocities, where the ejection of steam from the grooves between the fins drives the heat transfer. In this range we see 10 - 20Hz oscillations in the water pressure which correspond to the ejection frequency.

- At high flow velocity the vortices are sufficiently violent to supply cold water into the grooves and the heat transfer is sufficiently large to avoid the formation of larger steam bubbles.

The advantages of a finned structure are:

- the increase of the heat transfer surface by the fins,

- the thermal inertia, which the cold fins provide in the case of a local burnout,

- turbulence is only created where it is needed to improve the heat transfer

- the water flow rate can be adjusted to the requirements by the width of the water channel.

7. Test Results from Beryllium tiles brazed onto CuCrZr Copper

Beryllium tiles have been brazed onto our standard vapotron element with a cross section of 500 x 27 mm². The beryllium tiles were 2 and 3 mm thick with different castellations. Sheer tests showed a strength of the brazed joint of 170 - 200 N/mm². The elements were, as foreseen in the divertor, rigidly fixed to a strong back which prevents movement due to thermal expansion. The test was carried out using modulated beams with on/off periods of equal llength. The tiles were castellated into 6 x 6 mm², or 27 x 6 mm², or 27 x 27 mm² sections with the castellations penetrating either the full or half the thickness. Independent of the degree of castellation the tiles became detached when the power density exceeded 16 MW/m². This can be

Fig. 22: Be tiles after the test

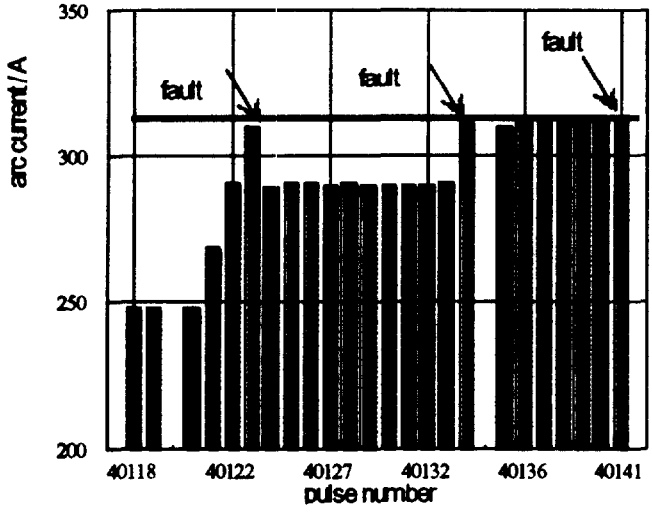

Fig. 23: Fault sequence for the B-Ag-18 braze. A fault develops, when the arc current exceeds 320 A. The arc current is proportional to the initial power density

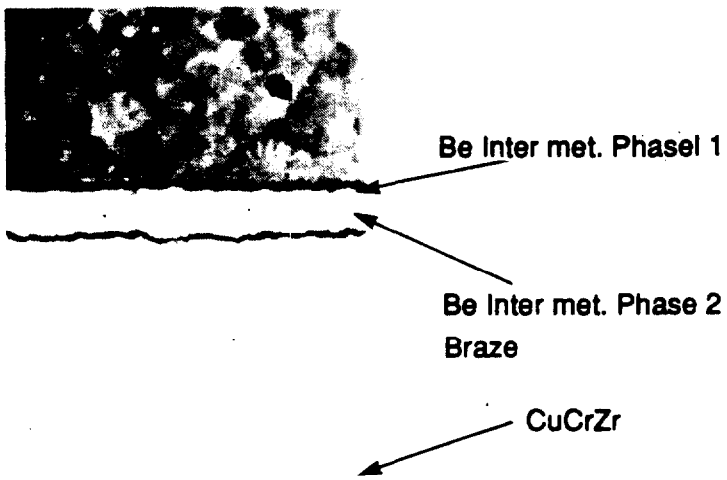

JG92.428/2

Fig. 24: Micrograph of the braze. Small cracks develop

clearly seen in Fig. 23. The faults are shown in Fig. 22, a photograph taken after the test.

Micrographs of the tiles after the test show (Fig. 24) that cracks develop in the inter-metallic layer between the braze and the Beryllium. This inter-metallic layer is very bridle (hardness 400 - 700 Vickers). Although the braze can withstand the average design loading of 12 MW/m² the safety margin is considered inadequate for an oscillating load. Alternative brazing procedures, which reduce the diffusion of Beryllium into the braze, are under investigation together with alternative bonding techniques such as plasma spaying, explosive bonding, or HIP-ing. Our tests confirmed, that it is indeed possible for the copper alloy to withstand the stresses generated by thermal expansion when the test element is rigidly supported.

References:

[1] P-H Rebut, Magnetic confinement Fusion: Recent Results at JET and Plans for the Future, JET-P(92)21, (preprint of an invited talk 3rd Eur. Part. Acc. Conf., Berlin, Germany, 24th - 28th March 1992 and M Huguet, Design of the JET Pumped Divertor, JET-P(91)51, preprint of a paper presented to the 14th Symp. on Fus. Eng., San Diego, USA, 30 Sept - 3rd Oct. 1991

[2] CH Beutheret, Perfectionnements aux dispositifs d'echange de chaleur entre une paroi et un liquide, French patent No 1, 502, 797, 16th Oct. 1967

[3] E Deksnis, Solid Beryllium Tiles for the JET pumped Divertor, this conference, paper1739-14

[4] H D Falter, Power Loading Tests of the JET Pumped Divertor Plates, Proceedings of the 16th Symp on Fus Techn, London U.K., 3-7 Sept. 1990, ISBN 0 444 88508 0, Elsevier Science Publishers B.V. 1991

[5] AGA Thermovision 782, AGA Infrared Systems AB, S 18211 Danderyd, Sweden

[6] Type 7201, Fisher Controls Ltd, Tylors Works, Victoria Road, Burgess Hill, Sussex RH15 9LJ, U.K.

[7] M N Özisik, Heat Transfer a basic approach, McGraw-Hill Book Company, New York, 1985

[8] C B Baxi, A Model for Analytical Performance Prediction of Hypervapotron, To be presented to 5 Int Topical Meeting on Nuclear Reactor Thermal Hydraulics, Salt Lake City, USA, 21-24 Sept. 1992

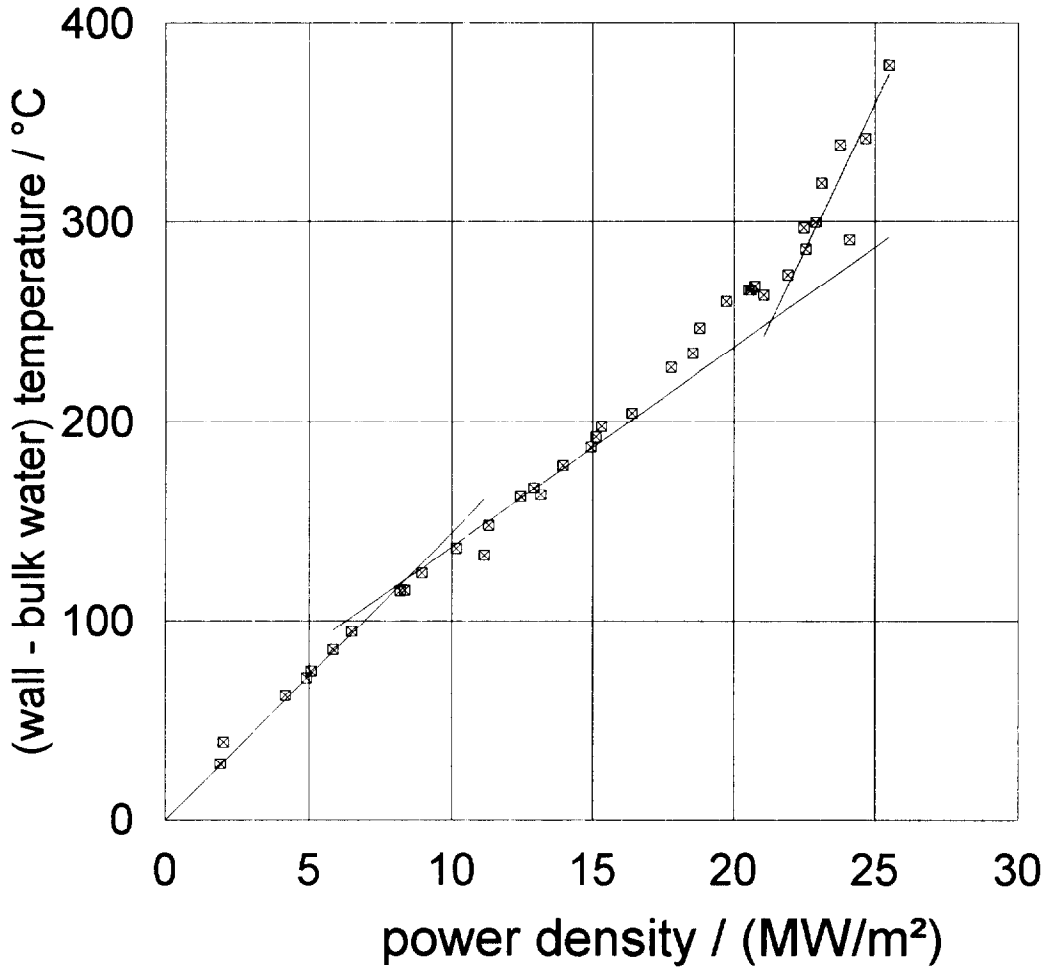
400
300
200
100
0
(wall - bulk water) temperature / °C
0
5
10
15
20
25
30
power density / (MW/m²)

ANNEX

P.-H. REBUT, A. GIBSON, M. HUGUET, J.M. ADAMS[1], B. ALPER, H. ALTMANN, A. ANDERSEN[2], P. ANDREW[3], M. ANGELONE[4], S. ALI-ARSHAD, P. BAIGGER, W. BAILEY, B. BALET, P. BARABASCHI, P. BARKER, R. BARNSLEY[5], M. BARONIAN, D.V. BARTLETT, L. BAYLOR[6], A.C. BELL, G. BENALI, P. BERTOLDI, E. BERTOLINI, V. BHATNAGAR, A.J. BICKLEY, D. BINDER, H. BINDSLEV[2], T. BONICELLI, S.J. BOOTH, G. BOSIA, M. BOTMAN, D. BOUCHER, P. BOUCQUEY, P. BREGER, H. BRELEN, H. BRINKSCHULTE, D. BROOKS, A. BROWN, T. BROWN, M. BRUSATI, S. BRYAN, J. BRZOZOWSKI[7], R. BUCHSE[22], T. BUDD, M. BURES, T. BUSINARO, P. BUTCHER, H. BUTTGEREIT, C. CALDWELL-NICHOLS, D.J. CAMPBELL, P. CARD, G. CELENTANO, C.D. CHALLIS, A.V. CHANKIN[8], A. CHERUBINI, D. CHIRON, J. CHRISTIANSEN, P. CHUILON, R. CLAESEN, S. CLEMENT, E. CLIPSHAM, J.P. COAD, I.H. COFFEY[9], A. COLTON, M. COMISKEY[10], S. CONROY, M. COOKE, D. COOPER, S. COOPER, J.G. CORDEY, W. CORE, G. CORRIGAN, S. CORTI, A.E. COSTLEY, G. COTTRELL, M. COX[11], P. CRIPWELL[12], O. Da COSTA, J. DAVIES, N. DAVIES, H. de BLANK, H. de ESCH, L. de KOCK, E. DEKSNIS, F. DELVART, G.B. DENNE-HINNOV, G. DESCHAMPS, W.J. DICKSON[13], K.J. DIETZ, S.L. DMITRENKO, M. DMITRIEVA[14], J. DOBBING, A. DOGLIO, N. DOLGETTA, S.E. DORLING. P.G. DOYLE, D.F. DÜCHS, H. DUQUENOY, A. EDWARDS, J. EHRENBERG, A. EKEDAHL, T. ELEVANT[7], S.K. ERENTS[11], L.G. ERIKSSON, H. FAJEMIROKUN[12], H. FALTER, J. FREILING[15], F. FREVILLE, C. FROGER, P. FROISSARD, K. FULLARD, M. GADEBERG, A. GALETSAS, T. GALLAGHER, D. GAMBIER, M. GARRIBBA, P. GAZE, R. GIANNELLA, R.D. GILL, A GIRARD, A. GONDHALEKAR, D. GOODALL[11], C. GORMEZANO, N.A. GOTTARDI, C. GOWERS, B.J. GREEN, B. GRIEVSON, R. HAANGE, A. HAIGH, C.J. HANCOCK, P.J. HARBOUR, T. HARTRAMPF, N.C. HAWKES[11], P. HAYNES[11], J.L. HEMMERICH, T. HENDER[11], J. HOEKZEMA, D. HOLLAND, M. HONE, L. HORTON, J. HOW, M. HUART, I. HUGHES, T.P. HUGHES[10], M. HUGON, Y. HUO[16], K. IDA[17], B. INGRAM, M. IRVING, J. JACQUINOT, H. JAECKEL, J.F. JAEGER, G. JANESCHITZ, Z. JANKOVICZ[18], O.N. JARVIS, F. JENSEN, E.M. JONES, H.D. JONES, L.P.D.F. JONES, S. JONES[19], T.T.C. JONES, J.-F. JUNGER, F. JUNIQUE, A. KAYE, B.E. KEEN, M. KEILHACKER, G.J. KELLY, W. KERNER, A. KHUDOLEEV[21], R. KONIG, A. KONSTANTELLOS, M. KOVANEN[20], G. KRAMER[15], P. KUPSCHUS, R. LÄSSER, J.R. LAST, B. LAUNDY, L. LAURO-TARONI, M. LAVEYRY, K. LAWSON[11], M. LENNHOLM, J. LINGERTAT[22], R.N. LITUNOVSKI, A. LOARTE, R. LOBEL, P. LOMAS, M. LOUGHLIN, C. LOWRY, J. LUPO, A.C. MAAS[15], J. MACHUZAK[19], B. MACKLIN, G. MADDISON[11], C.F. MAGGI[23], G. MAGYAR, W. MANDL[22], V. MARCHESE, G. MARCON, F. MARCUS, J. MART, D. MARTIN, E. MARTIN, R. MARTIN-SOLIS[24], P. MASSMANN, G. MATTHEWS, H. McBRYAN, G. McCRACKEN[11], J. McKIVITT, P. MERIGUET, P. MIELE, A. MILLER, J. MILLS, S.F. MILLS, P. MILLWARD, P. MILVERTON, E. MINARDI[4], R. MOHANTI[25], P.L. MONDINO, D. MONTGOMERY[26], A. MONTVAI[27], P. MORGAN, H. MORSI, D. MUIR, G. MURPHY, R. MYRNÄS[28], F. NAVE[29], G. NEWBERT, M. NEWMAN, P. NIELSEN, P. NOLL, W. OBERT, D. O'BRIEN, J. ORCHARD, J. O'ROURKE, R. OSTROM, M. OTTAVIANI, M. PAIN, F. PAOLETTI, S. PAPASTERGIOU, W. PARSONS, D. PASINI, D. PATEL, A. PEACOCK, N. PEACOCK[11], R.J.M. PEARCE, D. PEARSON[12], J.F. PENG[16], R. PEPE DE SILVA, G. PERINIC, C. PERRY, M. PETROV[21], M.A. PICK, J. PLANCOULAINE, J.-P POFFÉ, R. PÖHLCHEN, F. PORCELLI, L. PORTE[13], R. PRENTICE, S. PUPPIN, S. PUTVINSKII[8], G. RADFORD[30], T. RAIMONDI, M.C. RAMOS DE ANDRADE, R. REICHLE, J. REID, S. RICHARDS, E. RIGHI, F. RIMINI, D. ROBINSON[11], A. ROLFE, R.T. ROSS, L. ROSSI, R. RUSS, P. RUTTER, H.C. SACK, G. SADLER, G. SAIBENE, J.L. SALANAVE, G. SANAZZARO, A. SANTAGIUSTINA, R. SARTORI, C. SBORCHIA, P. SCHILD, M. SCHMID, G. SCHMIDT[31], B. SCHUNKE, S.M. SCOTT, L. SERIO, A SIBLEY, R. SIMONINI, A.C.C. SIPS, P. SMEULDERS, R. SMITH, R. STAGG, M. STAMP, P. STANGEBY[3], R. STANKIEWICZ[32], D.F. START, C.A. STEED, D. STORK, P.E. STOTT, P. STUBBERFIELD, D. SUMMERS, H. SUMMERS[13], L. SVENSSON, J.A. TAGLE[33], M. TALBOT, A. TANGA, A. TARONI, C. TERELLA, A TERRINGTON, A TESINI, P.R. THOMAS, E. THOMPSON, K. THOMSEN, F. TIBONE, A. TISCORNIA, P. TREVALION, B. TUBBING, P. VAN BELLE, H. VAN DER BEKEN, G. VLASES, M. VON HELLERMANN, T. WADE, C. WALKER, R. WALTON[31], D. WARD, M.L. WATKINS, N. WATKINS, M.J. WATSON, S. WEBER[34], J. WESSON, T.J. WIJNANDS, J. WILKS, D. WILSON, T. WINKEL, R. WOLF, D. WONG, C. WOODWARD, Y. WU[35], M. WYKES, D. YOUNG, I.D. YOUNG, L. ZANNELLI, A. ZOLFAGHARI[19], W. ZWINGMANN

[1] Harwell Laboratory, UKAEA, Harwell, Didcot, Oxfordshire, UK.
[2] Risø National Laboratory, Roskilde, Denmark.
[3] Institute for Aerospace Studies, University of Toronto, Downsview, Ontario, Canada.
[4] ENEA Frascati Energy Research Centre, Frascati, Rome, Italy.
[5] University of Leicester, Leicester, UK.
[6] Oak Ridge National Laboratory, Oak Ridge, TN, USA.
[7] Royal Institute of Technology, Stockholm, Sweden.
[8] I.V. Kurchatov Institute of Atomic Energy, Moscow, Russian Federation.
[9] Queens University, Belfast, UK.
[10] University of Essex, Colchester, UK.
[11] Culham Laboratory, UKAEA, Abingdon, Oxfordshire, UK.
[12] Imperial College of Science, Technology and Medicine, University of London, London, UK.
[13] University of Strathclyde, Glasgow, UK.
[14] Keldysh Institute of Applied Mathematics, Moscow, Russian Federation.
[15] FOM-Institute for Plasma Physics "Rijnhuizen", Nieuwegein, Netherlands.
[16] Institute of Plasma Physics, Academia Sinica, Hefei, Anhui Province, China.
[17] National Institute for Fusion Science, Nagoya, Japan.
[18] Soltan Institute for Nuclear Studies, Otwock/Świerk, Poland.
[19] Plasma Fusion Center, Massachusetts Institute of Technology, Boston, MA, USA.
[20] Nuclear Engineering Laboratory, Lappeenranta University, Finland.
[21] A.F. Ioffe Physico-Technical Institute, St. Petersburg, Russian Federation.
[22] Max-Planck-Institut für Plasmaphysik, Garching, Germany.
[23] Department of Physics, University of Milan, Milan, Italy.
[24] Universidad Complutense de Madrid, Madrid, Spain.
[25] North Carolina State University, Raleigh, NC, USA.
[26] Dartmouth College, Hanover, NH, USA.
[27] Central Research Institute for Physics, Budapest, Hungary.
[28] University of Lund, Lund, Sweden.
[29] Laboratorio Nacional de Engenharia e Tecnologia Industrial, Sacavem, Portugal.
[30] Institute of Mathematics, University of Oxford, Oxford, UK.
[31] Princeton Plasma Physics Laboratory, Princeton University, Princeton, NJ, USA.
[32] RCC Cyfronet, Otwock/Świerk, Poland,
[33] Centro de Investigaciones Energéticas, Medioambientales y Tecnológicas, Madrid, Spain.
[34] Freie Universität, Berlin, Germany.
[35] Insitute for Mechanics, Academia Sinica, Beijing, China.